UW-Madison.
SSEC Publication No.94.04.A1.

Space Science and Engineering Center
University of Wisconsin–Madison

Madison, WI 53706

DISCRIMINATING CLEAR SKY FROM CLOUD WITH MODIS ALGORITHM THEORETICAL BASIS DOCUMENT

A REPORT from the

COOPERATIVE INSTITUTE FOR METEOROLOGICAL SATELLITE STUDIES

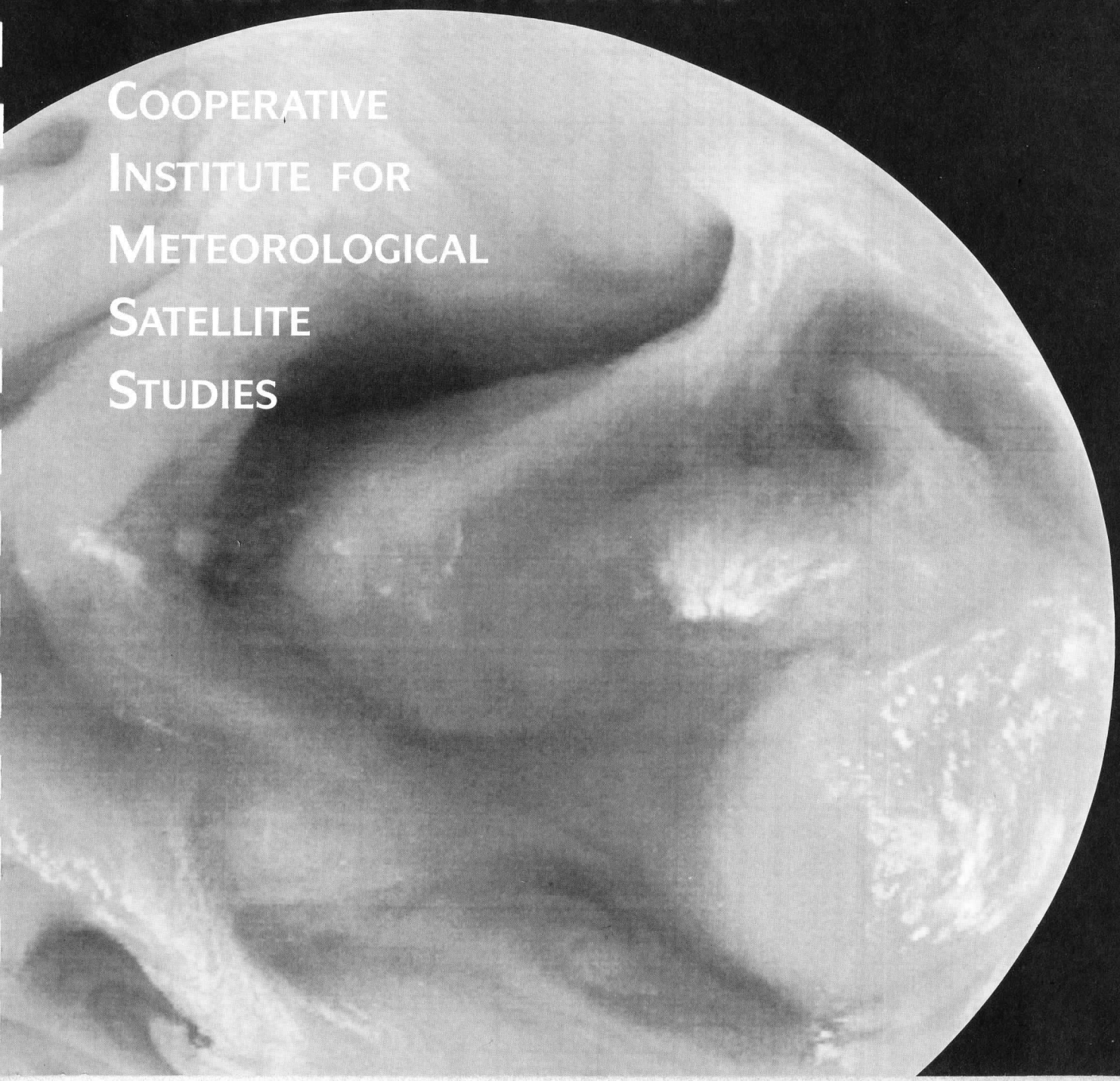

The Schwerdtfeger Library
1225 W. Dayton Street
Madison, WI 53706

DISCRIMINATING CLEAR SKY FROM CLOUD WITH MODIS ALGORITHM THEORETICAL BASIS DOCUMENT

Steve Ackerman
Chris Moeller
Kathleen Strabala
Cooperative Institute for Meteorological Satellite Studies
University of Wisconsin - Madison
Madison, WI

Bryan Baum
NASA/LaRC
Hampton, VA

Ron Welch
Institute of Atmospheric Sciences
South Dakota School of Mines and Technology
Rapid City, SD

Paul Menzel
NOAA/NESDIS
University of Wisconsin - Madison
Madison, WI

version 1

April 1994

Table of Contents

1.0 Introduction

Clouds are generally characterized by higher reflectance and lower temperature than the underlying earth surface. As such, simple visible and infrared window threshold approaches offer considerable skill in cloud detection. However there are many surface conditions when this characterization of clouds is inappropriate, most notably over snow and ice. Additionally, some cloud types such as cirrus, low stratus, and small cumulus are difficult to detect because of insufficient contrast with the surface radiance. Cloud edges cause further difficulty since the MODIS field of view will not always be completely cloudy or clear. The 36 channel MODIS offers the opportunity for multispectral approaches to cloud detection so that many of these concerns can be mitigated; additionally, spatial uniformity tests offer confirmation of cloudy or clear sky conditions.

This document describes algorithms for cloud detection and details the MODIS applications. The algorithm has been drafted in close collaboration with members of the CERES Science Team. Several relevant references are listed below for further reading regarding cloud detection; a more extensive listing is included in section 4.0.

Ackerman, S. A., W. L. Smith and H. E. Revercomb, 1990: The 27-28 October 1986 FIRE IFO cirrus case study: spectral properties of cirrus clouds in the 8-12 micron window. Mon. Wea. Rev., 118, 2377-2388.

Coakley, J. A. and F. P. Bretherton, 1982: Cloud cover from high-resolution scanner data: Detecting and allowing for partially filled fields of view. J. Geophys. Res., 87, 4917-4932.

Ebert, E., 1989: Analysis of polar clouds from satellite imagery using pattern recognition and a statistical cloud analysis scheme. J. Appl. Meteor., 28, 382-399.

Gao, B.-C., A. F. H. Goetz, and W. J. Wiscombe, 1993: Cirrus cloud detection from airborne imaging spectrometer data using the 1.38 micron water vapor band. Geophys. Res. Letter, 20, no. 4, 301-304.

Garand, L., 1988: Automated recognition of oceanic cloud patterns. Part I: Methodology and application to cloud climatology. J. Climate, 1, 20-39.

Inoue, T., 1987: A cloud type classification with NOAA 7 split window measurements. J. Geophys. Res., 92, 3991-4000.

Kaufman, Y. J., 1987: Satellite sensing of aerosol absorption. J. Geophys. Res., 92, 4307-4317.

Kaufman, Y. J., and C. Sendra, 1988: Algorithm for atmospheric corrections of visible and near IR satellite imagery. Int. J. Remote Sens., 9, 1357-1381.

King, M. D., Y. J. Kaufman, W. P. Menzel and D. Tanre, 1992: Remote sensing of cloud, aerosol, and water vapor properties from the Moderate Resolution Imaging Spectrometer (MODIS). IEEE Trans. Geosci. Remote Sensing, 30, 2-27.

Menzel, W. P., D. P. Wylie, and K. I. Strabala, 1992: Seasonal and Diurnal Changes in Cirrus Clouds as seen in Four Years of Observations with the VAS. J. Appl. Meteor., 31, 370-385.

Rossow, W. B. and L. C. Garder, 1993: Cloud detection using satellite measurements of infrared and visible radiances for ISCCP. J. Climate, 6, 2341-2369.

Stowe, L. L., E. P. McClain, R. Carey, P. Pellegrino, G. Gutman, P. Davis, C. Long, and S. Hart, 1991: Global distribution of cloud cover derived from NOAA/AVHRR operational satellite data. Adv. Space Res., 11, 51-54.

Strabala, K. I., S. A. Ackerman, and W. P. Menzel, 1994: Cloud Properties Inferred from 8-12μm Data. J. Appl. Meteor., 33, 212-229.

Welch, R. M., S. K. Sengupta, A. K. Goroch, P. Rabindra, N. Rangaraj, and M. S. Navar, 1992: Polar cloud and surface classification using AVHRR imagery: An intercomparison of methods, J. Appl. Meterol., 31, 405-420.

Wylie, D. P., W. P. Menzel, H. M. Woolf, and K. I. Strabala, 1994: Four Years of Global Cirrus Cloud Statistics Using HIRS. accepted by J. Clim.

Yamanouchi, T., K. Suzuki, and S. Kawaguci, 1987: Detection of clouds in Antarctica from infrared multispectral data of AVHRR. J. Meteor. Soc. Japan, 65, 949-962.

2.0 Overview

2.1 Objective

The MODIS cloud mask will indicate whether a given field of view has an unobstructed view of the earth surface and additionally whether that clear view is affected by cloud shadows. The cloud mask will be generated at the three resolutions of the MODIS data (250 meter, 500 meter, and 1000 meter). Input to the cloud mask algorithms is assumed to be calibrated and navigated level 1B data; additionally, the MODIS data is assumed to be meeting specification so that no accommodation for striping is being made. The cloud mask will be determined for good data only (ie. fields of view where the data in the cloud mask channels 1, 2, 6, 8, 19, 22, 26, 27, 29, 31, 32, and 35 have radiometric integrity); incomplete or bad data will create holes in the cloud mask.

Several points need to be made regarding the approach to the MODIS cloud mask that has been adopted for this ATBD. (1) The cloud mask is not the final cloud product from MODIS; individual PIs have the responsibility to deliver algorithms for various cloud parameters. If it is more efficient or desirable to include some of the PI algorithms during the cloud mask processing, that can be done. (2) The cloud mask ATBD is assuming that calibrated quality controlled data is the input and a simple cloud mask is the output. The overall template for the MODIS data processing must be planned at the project level as must the coordination of the cloud mask with the activities that will be producing calibrated level 1B data.

2.2 Background

The MODIS cloud algorithm will benefit from previous work to characterize global cloud cover. The International Satellite Cloud Climatology Project (ISCCP) has developed cloud detection schemes using visible and infrared window radiances. The NOAA Cloud Advanced Very High Resolution Radiometer (CLAVR) algorithm uses the five visible and infrared channels of the AVHRR for cloud detection using spectral and spatial variability tests. CO_2 Slicing characterizes global high cloud cover, including thin cirrus, using infrared radiances in the carbon dioxide sensitive portion of the spectrum. Additionally, spatial coherence of infrared radiances in cloudy and clear skies has been used successfully in regional cloud studies. The following paragraphs summarize these prior approaches briefly.

The International Satellite Cloud Climatology Project (ISCCP) cloud masking algorithm is described by Rossow (1989, 1993), Rossow et al. (1989) and Seze and Rossow (1991). Only two channels are used, the narrowband visible (0.6 micron) and the infrared window (11 micron). Each observed radiance value is compared against its corresponding Clear-Sky Composite value. Clouds are assumed to be detected only when they alter the radiances by more than the uncertainty in the clear values. In this way the "threshold" for cloud detection is the magnitude of the uncertainty in the clear radiance estimates.

The ISCCP algorithm is based on the premise that the observed VIS and IR radiances are caused by only two types of conditions, 'cloudy' and 'clear', and that the ranges of radiances and their variability that are associated with these two conditions do not overlap (Rossow and Garder 1993). As a result, the algorithm is based upon thresholds, where a pixel is classified as "cloudy" only if at least one radiance value is distinct from the inferred "clear" value by an amount larger than the uncertainty in that "clear" value. The uncertainty can be caused both by measurement errors and by natural variability. This algorithm is constructed to be "cloud-conservative," minimizing false cloud detections but missing clouds that resemble clear conditions.

The ISCCP cloud-detection algorithm consists of five steps (Rossow and Garder 1993): (1) space contrast test on a single IR image; (2) time contrast test on three consecutive IR images at constant diurnal phase; (3) cumulation of space/time statistics for IR and VIS images; (4) construction of clear-sky composites for IR and VIS every 5 days at each diurnal phase and location; and (5) radiance threshold for IR and VIS for each pixel.

The NOAA CLAVR algorithm (Phase I) uses all five channels of AVHRR (.63, .86, 3.7, 11.0, 12.0 micron) to derive a global cloud mask (Stowe et al., 1991). It examines multispectral information, channel

differences, and spatial differences and then employs a series of sequential decision tree tests. Cloudfree, mixed (variable cloudy) and cloudy regions are identified for 2x2 global area coverage (GAC) pixel (4 km resolution) arrays. If all four pixels in the array fail all the cloud tests, then the array is labeled as cloud-free (0% cloudy); if all four pixels satisfy just one of the cloud tests, then the array is labeled as 100% cloudy. If 1 to 3 pixels satisfy a cloud test, then the array is labeled as mixed and assigned an arbitrary value of 50% cloudy. If all four pixels of a mixed or cloudy array satisfy a clear-restoral test (required for snow/ice, ocean specular reflection, and bright desert surfaces) then the pixel array is re-classified as "restored-clear" (0% cloudy). The set of cloud tests is subdivided into daytime ocean scenes, daytime land scenes, nighttime ocean scenes and nighttime land scenes.

Subsequent phases of CLAVR, now under development, will use dynamic clear/cloud thresholds predicted from the angular pattern observed from the clear sky radiance statistics of the previous 9-day repeat cycle of the NOAA satellite for a mapped one degree equal area grid cell (Stowe et al., 1994). As a further modification, CLAVR will include pixel by pixel classification based upon different threshold tests to separate clear from cloud contaminated pixels, and to separate cloud contaminated pixels into partial and total (overcast) cover. Cloud contaminated pixels will be radiatively "typed" as belonging to low stratus, thin cirrus, and deep convective cloud systems. A fourth type indicates all other clouds, including mixed level clouds.

CO_2 slicing (Wylie et al., 1994) has been used to distinguish transmissive clouds from opaque clouds and clear sky using High resolution Infrared Radiation Sounder (HIRS) multispectral observations. With radiances around the broad CO_2 absorption band at 15 microns, clouds at various levels of the atmosphere can be detected. Radiances from near the center of the absorption band are sensitive to only upper levels while radiances from the wings of the band (away from the band center) see successively lower levels of the atmosphere. The CO_2 slicing algorithm determines both cloud level and cloud amount from radiative transfer principles. It has been shown to be especially effective for detecting thin cirrus clouds that are often missed by simple infrared window and visible approaches. Difficulties arise when the spectral cloud forcing (clear minus cloudy radiance for a spectral band) is less than the instrument noise.

The spatial coherence method (Coakley and Bretherton, 1982) is especially useful in determining clear and cloudy sky radiances over uniform backgrounds. It is applicable to single-layered and sometimes multi-layered cloud systems that extend over moderately large regions, greater than $(250\ km)^2$, and which have completely cloudy and completely clear pixels. Using the local spatial structure of the IR radiances, a plot of standard deviation versus mean radiance often produces an arch-shaped structure where the feet with low standard deviations are associated with clear sky for high mean values and cloudy conditions for low mean values. The spatial coherence test is not run over regions of varying topography; however, it is applied for relatively homogeneous topographical regions of similar ecosystem.

The above algorithms are noted as they have been incorporated into current global cloud climatologies. Other studies (see the reference list) of cloud detection which focus on a method or geographic region have also influenced this draft of the ATBD. The MODIS cloud mask algorithm will build on this work, but will have considerable advantage because it has multispectral information and high spatial resolution. Of the 36 spectral channels available, twelve visible and infrared radiances will be used to mitigate some of the difficulties experienced by the previous algorithms. MODIS has 250 meter resolution in two of the visible channels, 500 meter resolution in four of the visible channels, and 1000 meter resolution in the remaining channels. The MODIS adaptation of spatial coherence techniques will take advantage of the high spatial resolution of the MODIS data; spatial coherence will be investigated on much smaller areas than before, probably 5 km x 5 km.

The Schwerdtfeger Library
1225 W. Dayton Street
Madison, WI 53706

2.3 MODIS Characteristics

The MODIS channels that will be used in the cloud algorithm are indicated in Table 1.

Table 1. Channels used in generation of MODIS cloud mask.

Channel Number	Wavelength (microns)	Used in Cloud Mask (B indicates backup to another channel)
Reflected radiation		
1	0.659	Y
2	0.865	Y
3	0.470	N
4	0.555	B
5	1.240	N
6	1.640	Y
7	2.130	N
8	0.415	Y
9	0.443	N
10	0.490	N
11	0.531	N
12	0.565	N
13	0.653	N
14	0.681	N
15	0.750	N
16	0.865	N
17	0.905	N
18	0.936	N
19	0.940	Y?
26	1.375	Y
20, 21	3.750	B
22	3.959	Y
23	4.050	N
24	4.465	N
25	4.515	B
Emitted radiation		
20, 21	3.750	B
22	3.959	Y
23	4.050	N
24	4.465	N
25	4.515	B
27	6.715	Y
28	7.325	N?
29	8.550	Y
30	9.730	N
31	11.030	Y
32	12.020	Y
33	13.335	N
34	13.635	N
35	13.935	Y
36	14.235	N

2.4 Inputs and Outputs

The following paragraphs summarize the input and output of the MODIS cloud algorithm. Details on the multispectral single field of view and spatial coherence algorithms are found in the section on algorithm description.

Several inputs are required for the cloud mask; they are:

* sun angle, azimuthal angle, and viewing angle
* land/water map at 1 km resolution
  (MODIS will develop a better one subsequently)
* topography at 10 minute resolution
  (Navy character map will provide this;
  as well as rugged versus plateau terrain)
* ecosystems at 10 minute resolution
  (map of 59 classes of ecosystems available)
* snow/ice from yesterday known at 1 km resolution
  (ancillary sea versus land discrimination at 18 km res)
* surface temperatures (sea and land) at 1 degree resolution
  (NMC analysis or yesterdays MODIS observations)

The output of the MODIS cloud mask algorithm will be a 24 bit word for each field of view. The contents are indicated in Table 2.

Table 2. MODIS cloud mask contents for each field of view.

bit	content
summary of all algorithms	
1	obstructed fov (yes/no)
2	quality flag
ancillary information	
1	snow/ice
2	land/water
1	sunglint found (yes/no)
results from classes of cloud algorithms	
1	IR threshold found cloud
1	IR temperature differences found cloud
1	vis threshold found cloud
1	vis ratio found cloud
1	near infrared thin cirrus test found cloud
1	CO_2 high cloud test found cloud
1	IR spatial tests found cloud
1	vis spatial tests found cloud
1	multiple layers identified
1	cloud shadow found
1	1.6μm found cloud
room for additional information	
6	spare

Smoke from forest fires, dust storms over deserts, and other aerosols that result in obstructing the field of view between the surface and the satellite will be considered as "cloud" if such pixels pass the threshold tests. Examples are briefly presented in section 3.1.14. When new tests are developed that distinguish between these phenomena, they will be incorporated into the algorithm.

Not included in the output, but possibly generated in the cloud mask processing is information on

* cloud fraction (at 1 km)
* surface texture
* water fraction in fov (at 1 km)
* aerosol presence
* temporal continuity of cloud cover

3.0 Algorithm Description

The theoretical basis of the algorithms and practical considerations are contained in this section. For nomenclature, we shall denote the satellite measured visible (VIS) reflectance as r, and refer to the infrared (IR) radiance as brightness temperature (equivalent blackbody temperature using the Planck function) denoted as BT. Subscripts refer to the wavelength at which the measurement is made.

3.1 Theoretical Description of Cloud Detection

This section will discuss the physics of detecting clouds from multispectral visible and infrared radiances from a given field of view (FOV) or an array of FOVs, present the application with MODIS data, and indicate various problem areas. Cloud detection using visible radiances is presented first, then infrared detection including spatial coherence algorithms, and finally automated approaches using fuzzy logic.

3.1.1 Reflectance Uniformity Test

The reflectance uniformity test (borrowed from CLAVR) is applied by computing the maximum and minimum values of MODIS channel 1 (.66 micron) or channel 2 (.87 micron) reflectances within a 5 km x 5 km pixel array. Pixel arrays with channel 1 reflectance differences greater than threshold 1 (around 9%) over land or channel 2 reflectance differences greater than threshold 2 (possibly 0.3%) over ocean are labeled as mixed (Stowe et al., 1993). The value over ocean is low because a cloud-free ocean is almost uniformly reflective, while non-uniformity is assumed to be caused by cloudiness. This test will be refined for MODIS applications; first, by requiring that the ecosystem be the same for the pixel array. Second, the mean and standard deviation of reflectance values for each of the 59 ecosystems (identified in section 3.2.1) will be computed as a function of season. And third, the reflectance threshold will be a function of satellite zenith and view angle.

3.1.2 Reflectance Ratio Test

The reflectance ratio test uses channel 2 divided by channel 1 ($r_{.87}/r_{.66}$). For cloudy regions this channel ratio is between 0.9 and 1.1. This ratio provides an indicator for the presence of clouds. If the ratio falls with this range, further tests should be performed to test for cloud. New analyses (McClain, 1993) suggest that the minimum value may need to be lowered to about 0.8, at least for some cases. For cloud-free ocean, the ratio is expected by be less than 0.75 (Saunders and Kriebel, 1988).

3.1.3 Reflectance Threshold Test

The reflectance threshold test uses channel 22 (3.9 micron) where values > 6% are considered to be cloudy. However, "cloudy" pixels with channel 22 reflectance values < 3% are considered to be snow/ice (Stowe et al., 1994). Note that the channel 22 reflectance tests are not applied over deserts. This is because bright desert regions with highly variable emissivities tend to be classified incorrectly as cloudy with this test. Thermal contrast needs to be examined in conjunction with channel 22 reflectivity. As experience indicates with these approaches, the actual thresholds will be adjusted to ecosystem type.

3.1.4 Near Infrared Thin Cirrus Test

This is a new approach to cirrus detection suggested by the work of Gao et al. (1993); it is still under development. The MODIS channel 26 (1.38 micron) will use reflectance thresholds to detect the presence of thin cirrus cloud in the upper troposphere under daytime viewing conditions. The strength of this cloud detection channel lies in the strong water vapor absorption in the 1.38 micron region (see Figure 1). With sufficient atmospheric water vapor present (estimated to be about 0.4 cm precipitable water) in the beam path, no upwelling reflected radiance from the earth's surface reaches the satellite. The transmittance is given by

$$\tau(p_{sfc}) = \exp(-\delta_{H2O} * \sec\theta_o + -\delta_{H2O} * \sec\theta)$$

$$\delta_{H2O} = k_{H2O}\, du$$

As $\tau(p_{sfc}) \Rightarrow 0$, $L_{sfc} \Rightarrow 0$. τ is the two-way atmospheric transmittance from the top of the atmosphere down to the surface and back to the top of the atmosphere, δ_{H2O} is the water vapor optical depth, θ_o and θ are the solar and viewing zenith angles respectively, k is the water vapor absorption coefficient, u is the water vapor pathlength and L_{sfc} is the surface radiance reaching the sensor. Since 0.4 cm is a low atmospheric water content, most of the earth's surface will indeed be obscured in this channel. With relatively little of the atmosphere's moisture located high in the troposphere, high clouds appear bright and unobscured in the channel; reflectance from low and mid level clouds is partially attenuated by water vapor absorption.

Simple low and high reflectance (normalized by incoming solar at the top of the atmosphere) thresholds will be used to separate thin cirrus from clear and thick (near infrared cloud optical depth > ~ 0.2) cloud scenes. These thresholds will be set initially using a multiple-scattering model with the assumption of no surface reflectance contribution to the satellite observed radiance, i.e. - a dark background. New injections of volcanic aerosols into the stratosphere may impact the test result. Any ambiguity of high thin versus low or mid level thick cloud will be resolved by a test on the cloud height using a CO_2 sensitive MODIS channel 35 (see section 3.1.7).

The initial reflectance thresholds will be adjusted using inflight data (clear air radiance map) after MODIS is launched.

3.1.5 Infrared Window Brightness Temperature Threshold and Difference (BTD) Tests

Several infrared window threshold and temperature difference techniques are presented. They are most effective at night over water and must be used with caution in other situations. The first infrared (IR) test to apply over the oceans is a threshold test. For example, over open ocean if the brightness temperature in the 11 micron channel 31 (BT_{11}) is less than 270 K, we can safely assume a cloud is present. As a result of the relative spectral uniformity of surface emittance in the IR, spectral tests within various atmospheric windows (such as channels 29, 31, 32 at 8.6, 11, and 12 microns respectively) can be used to detect the presence of a cloud/aerosol. Differences between BT_{11} and BT_{12} have been widely used for cloud screening with AVHRR measurements and this technique is often referred to as the split window technique.

The basis of the split window technique for cloud detection lies in the differential water vapor absorption that exists between two window channels (8.6 and 11 micron and 11 and 12 micron) bandwidths. These spectral regions are considered to be part of the atmospheric window, where absorption is relatively weak (Figure 2). Most of the absorption lines are a result of water vapor molecules, with a minimum occurring around 11 microns. Since the absorption is weak, BT_{11} can be corrected for moisture absorption by adding the scaled brightness temperature difference of two spectrally close channels with different water vapor absorption coefficients; the scaling coefficient is a function of the differential water vapor absorption between the two channels. This is the basis for sea surface temperature retrieval.

The surface temperature, T_S, can be determined from observed remote sensing instruments if corrected for water vapor absorption effects

$$T_s = BT_{11} + \Delta BT$$

where BT_{11} is a window channel brightness temperature. To start with, the radiative transfer equation in a clear atmosphere can be written

$$R_{\lambda,clr} = B_\lambda(T(p_s))\tau_\lambda(p_s) + \int_{p_s}^{p_0} B_\lambda(T(p))\frac{d\tau_\lambda(p)}{dp}dp.$$

As noted above, absorption is relatively weak across the window region so that a linear approximation is made to the transmittance

$$\tau \approx 1 - k_\lambda u$$

Here k is the absorption coefficient of water vapor and u is the path length. The differential transmittance then becomes

$$d\tau_\lambda = -k_\lambda du.$$

Inserting this approximation into the window region radiative transfer equation will lead to

$$R_{\lambda,clr} = B_{\lambda,s}(1 - k_\lambda u_s) + k_\lambda \int_0^{u_s} \overline{B}_\lambda du.$$

Here, $\overline{B_\lambda}$ is the atmospheric mean Planck average. Since $B_{\lambda,s}$ will be close to both $R_{\lambda,clr}$ and $\overline{B_\lambda}$, we can linearize the radiative transfer equation with respect to T_S

$$BT_{b\lambda} = T_s(1 - k_\lambda u_s) + k_\lambda u_s \overline{BT}_\lambda$$

where $\overline{BT_\lambda}$ is the mean atmospheric temperature corresponding to $\overline{B_\lambda}$. For two window channels, you can ratio this equation, cancel out common factors and rearrange to end up with the following approximation

$$\frac{T_s - BT_{\lambda,1}}{T_s - BT_{\lambda,2}} = \frac{k_{\lambda,1}}{k_{\lambda,2}}.$$

Solving the equation for T_s yields

$$T_s = BT_{\lambda,1} + \frac{k_{\lambda,1}}{k_{\lambda,2} - k_{\lambda,1}}(BT_{\lambda,1} - BT_{\lambda,2}).$$

Thus, with a reasonable estimate of the sea surface temperature and total precipitable water, one can develop appropriate thresholds for cloudy sky. Such as

$$BT_{11} < 270 \text{ K}$$

$$BT_{11} + a_{PW} * (BT_{11}\text{-}BT_{12}) < SST$$

$$BT_{11} + b_{PW} * (BT_{11}\text{-}BT_{8.6}) < SST$$

where a_{PW} and b_{PW} are determined from a lookup table as a function of total precipitable water vapor (PW). This approach has been used operationally for 4 years for 8.6 and 11 micron bandwidths from the NOAA-10 and NOAA-12 and the 11 and 12 micron bandwidths from the NOAA-11, with a coefficient independent of PW (Menzel et al. 1993, Wylie et al. 1994).

To demonstrate this technique with observations, a global data set of collocated AVHRR GAC 11 and 12 micron and HIRS 8.6 and 11 micron scenes were collected and the total column PW estimated from integrated model mixing ratios to determine a direct regression between PW and the split window thresholds. Data was collected and regressions calculated from observations such as those depicted in Figure 3. The regressions were then modified for use with MODIS Airborne Simulator (MAS) bandwidths in TOGA/COARE data sets. Simulations and observations have shown the regression slopes to be consistent with those found for the AHVRR/HIRS clear scenes; however, the intercept values needed adjustment.

A disadvantage of the split window brightness temperature difference (BTD) approach is that water vapor absorption across the window is not linearly dependent on PW, thus second order relationships are sometimes used. The MODIS has a unique capability with the measurements at three wavelengths in the window, 8.6, 11 and 12 micron. The three spectral regions mentioned are very useful in determination of a cloud free atmosphere. This is because the index of refraction varies quite markedly over this spectral region for water, ice, and minerals common to many naturally occurring aerosols. As a result, the effect on the brightness temperature of each of the spectral regions is different, depending on the absorbing constituent. A depiction of this effect is summarized in Figure 4.

A tri-spectral combination of observations at 8.6, 11 and 12 micron bands was suggested for detecting cloud and cloud properties by Ackerman et al. (1990). Strabala et al. (1993) further explored this technique by utilizing very high spatial-resolution data from the MODIS Airborne Simulator (MAS). The physical premise of the technique is that ice and water vapor absorption peak in opposite halves of the window region; so that positive 8.6 minus 11 micron brightness temperature differences indicate cloud while negative differences, over oceans, indicate clear regions.

Analysis of MAS high spatial resolution (50 meter) data with all three 8.6, 11 and 12 micron bands reveal sharp delineation of differing cloud and background scenes, from which a simple automated threshold technique was developed as a MODIS prototype tri-spectral cloud detection algorithm (Strabala et al 1994). More rigorous techniques based on cluster analysis are presently being developed. The relationship between the two brightness temperature differences and clear sky have also been examined using collocated HIRS and AVHRR GAC global ocean data sets as depicted in Figure 5. As the atmospheric moisture increases, $BT_{8.6}$-BT_{11} decreases while BT_{11}-BT_{12} increases.

MODIS channel 22 (3.9 micron) also measures radiances in another window region near 3.5-4 microns so that the difference between BT_{11} and $BT_{3.9}$ can also be used to detect the presence of clouds. At night the

difference between the brightness temperatures measured in the shortwave (3.9 micron) and in the longwave (11 micron) window regions $BT_{3.9}$-BT_{11} can be used to detect partial cloud or thin cloud within the MODIS field of view. Small or negative differences are observed only for the case where an opaque scene (such as thick cloud or the surface) fills the field of view of the sensor. Negative differences occur at night over extended clouds due to the lower cloud emissivity at 3.9 microns.

Moderate to large differences result when a non-uniform scene (e.g., broken cloud) is observed. The different spectral response to a scene of non-uniform temperature is a result of Planck's law; the brightness temperature dependence on the warmer portion of the scene increasing with decreasing wavelength (the shortwave window Planck radiance is proportional to temperature to the thirteenth power, while the longwave dependence is to the fourth power). Differences in the brightness temperatures of the longwave and shortwave channels are small when viewing mostly clear or mostly cloudy scenes; however for intermediate situations the differences become large (greater than 3°C).

Cloud/aerosol masking over land surface from thermal infrared bands is more difficult than ocean due to potential variations in surface emittance. Nonetheless, simple thresholds can be established over certain land features. For example, over desert regions we can expect that $BT_{11} < 273$ K indicates cloud. Such simple thresholds will vary with ecosystem, season and time of day and are under investigation.

Brightness temperature difference testing can also be applied over land with careful consideration of variation in spectral emittance. For example, BT_{11}-$BT_{8.6}$ has large negative values over daytime desert and is driven to positive differences in the presence of cirrus. Some land regions have an advantage over the ocean regions because of the larger number of surface observations, which include air temperature, and vertical profiles of moisture and temperature. Further work on BTD applications over land scenes is forthcoming.

Infrared window tests at high latitudes are difficult. Distinguishing clear and cloud regions from satellite IR radiances is a challenging problem due to the cold surface temperatures. Yamanouchi et al. (1987) describe a nighttime polar (Antarctic) cloud/surface discrimination algorithm based upon brightness temperature differences between the AVHRR 3.7 and 11 micron channels and between the 11 and 12 micron channels. Their cloud/surface discrimination algorithm was more effective over water surfaces than over inland snow-covered surfaces. A number of problems arose over inland snow-covered surfaces. First, the temperature contrast between the cloud and snow surface became especially small, leading to a small brightness temperature difference between the two infrared channels. Second, the AVHRR channels are not well-calibrated at extremely cold temperatures (< 200 K). Under clear sky condition, surface radiative temperature inversions often exists. Thus, IR channels whose weighting function peaks down low in the atmosphere, will often have a larger BT than a window channel. For example $BT_{8.6} > BT_{11}$ in the presence of an inversion. The surface inversion can also be confused with thick cirrus cloud; this can be mitigated by other tests (e.g., the magnitude of BT_{11} or the BT_{11}-BT_{12}). Our analysis of BT_{11}-$BT_{6.7}$ has shown large negative difference over the Antarctic Plateau winter, which may be indicative of a strong surface inversion and thus clear skies. Further work is planned in this area.

3.1.6 Infrared Window One-Dimensional Histogram Tests

The infrared window histogram test is now presented; as with the threshold and BTD tests, it is most effective at night over water and must be used with caution in other situations. One-dimensional histogram tests have a long history of determining clear sky scenes and will be incorporated into the MODIS cloud mask. The method is physically based on the assumption that for a uniform scene, such as a small geographic region of the ocean, the observed radiances will be normally distributed, the width of the normal curve defined by the instrument noise. This test is not a single FOV test, but requires a number of observations over a given region with similar surface radiative properties. To improve the clear sky estimate, the histogram can be constructed only from the FOVs that pass one or more of the single FOV thresholds discussed above in section 3.1.5. A one-dimensional IR channel histogram is constructed over a given geographical region (5 km x 5 km). A gaussian function is fit to the warmest peak of the histogram; the temperature (BT_{peak}) and the noise limits (σ) are

determined. The clear sky brightness temperature threshold is the temperature that corresponds to one-sigma (σ) towards the cold side of the gaussian function peak.

$$BT_{thres} = BT_{peak} - \sigma$$

An example of this approach is demonstrated in Figure 6 using AVHRR global observations.

3.1.7 CO_2 Channel Test for High Clouds

The MODIS channel 35 (13.9 micron) provides good sensitivity to the relatively cold regions of the atmosphere. Only clouds above the 500 HPa will have strong contributions to the radiance to space observed at 13.9 microns; negligible contributions come from the earth surface. Thus a threshold test for cloud versus ambient atmosphere and a histogram test should reveal clouds above 500 HPa or high clouds. This test will be used in conjunction with the near infrared thin cirrus test (section 3.1.4).

3.1.8 Infrared Window Radiance Spatial Uniformity

The infrared window spatial uniformity test is also most effective at night over water and must be used with caution in other situations. Most ocean regions are well suited for spatial uniformity tests; such tests may be applied with less confidence in coastal regions or regions with large temperature gradients (e.g. the Gulf Stream.) Various spatial tests exist such as the spatial coherence and the ISCCP space contrast test. The spatial coherence test is based on the assumption of a uniform background and singled-layered, optically thick cloud systems. The emitted radiance is

$$I = (1 - A_c) I_{clr} - A_c I_{cld}$$

The method is based upon the computation of the mean and standard deviation for a group of pixels (e.g. 5 km x 5 km) using 11 micron radiances. When the standard deviation is plotted versus the mean an arch shaped structure is often observed. The warm pixels with low values of standard deviation are assumed to be clear regions. The clear sky FOVs can be selected as those within a standard deviation threshold (which is fixed at a small value) of the warm foot of the arch. Note that the derived clear sky foot of the arch should have a temperature consistent with the thresholds derived using the individual FOV tests.

The ISSCP space contrast (sc) test, described in Rossow and Garder (1993), is similar to that of spatial coherence and is physically based upon the fact that clear pixels tend to be warmer than cloudy pixels and exhibit less spatial variability. First for a small local region the pixel with the largest brightness temperature (BT_{11}^{max}) is found. All pixels colder than the spatial contrast ($BT_{11}^{max} - \Delta_{sc}$) value are labeled as cloudy; all others, including the warmest pixel are labeled as undecided. The size of the contrast threshold must be larger than the magnitude of natural variation at the surface and smaller than that caused by clouds. Values of Δ_{SC} near 3.5°C are common over ocean regions. Note that not only is it important that the class of pixels be identical, but also that the size of the region be chosen carefully. When extending into coastal regions and land regions containing mixed land and water, pixels are excluded from this test since the inherent contrast between land and water surface radiances would dominate the results. For regions that are too large, there is increased likelihood of spatial variations in surface parameters. The shape of the test regions also can be important, since meridional gradients in surface temperature generally are larger than zonal gradients.

Similar spatial tests will be incorporated into the MODIS cloud mask. The specific test will likely depend on how the data stream is structured regarding the ease of compositing pixels over geographic regions.

Uniform stratus can also give the appearance of a uniform ocean, thus the spatial tests must also be combined with spectral tests (e.g., the tri-spectral test.)

Surface temperature variability, both spatial and temporal, is larger over land than ocean, making land scene spatial uniformity tests difficult. ISCCP applies a space contrast test. MODIS spatial uniformity tests over land will be constrained to similar ecosystems in a given geographic regime. These tests have yet to be developed.

3.1.9 Infrared Window Plus Visible Threshold Tests

The IR single FOV tests (from section 3.1.5) can be combined with the visible tests (from the first four sections 3.1.1, 3.1.2, 3.1.3, and 3.1.4) and applied over the oceans during the daylight hours. FOVs that pass the visible tests can then be used to verify the IR thresholds derived in the nighttime. Daytime methods which include solar methods are constrained to solar zenith angles less than 85°. Sun glint occurs when the reflected sun angle, θ_r, lies between 0° and approximately 36°, where

$$\cos\theta_r = \sin\theta \sin\theta_\circ \cos\psi + \cos\theta\cos\theta_\circ$$

where $\theta_\circ$ is the solar zenith angle, θ is the viewing zenith angle, and ψ is the azimuthal angle. Sun glint is also a function of surface wind and sea state and so nighttime algorithms are often used in regions contaminated with sun glint.

Additionally during the day cloud detection can be accomplished by comparing brightness temperature differences between channel 20 (3.7 micron) and channel 22 (4.0 micron). The measured radiance from space can be estimated as

$$I_\lambda^{meas} = (1-r_\lambda)B_\lambda(T_{sfc}) + r_\lambda \int_{P_s}^{0} B_\lambda(T(P))dt_\lambda(P_\circ,P) - \int_{0}^{P_s} B_\lambda(T(P))dt_\lambda(0,P) + r_\lambda I_{\circ,\lambda}^{sun}(\theta_\circ,\psi)$$

where r_λ is the surface reflectance at the surface and $I_{\circ,\lambda}^{sun}$ is the downward solar radiance at the surface. The 3.7 micron channel will be contaminated by solar reflection to a much larger degree than the 4 micron observations. This allows a threshold such as

$$BT_{3.7} - BT_4 \le T_{\Delta sol}$$

3.1.10 Two-Dimensional Infrared and Visible Histogram Analysis

As with the 1-D histogram approach, 2-D histograms can be used which make use of the measurements of IR emitted radiances as well as the reflected solar visible radiances. A 2-D Gaussian surface can be fitted to the peak with the warmest temperature and/or lowest reflectance. The Gaussian surface equation is

$$G(IR,VIS) = G_{peak}\exp[-P(IR,VIS)]$$

where

$$P(IR,VIS) = \frac{(BT - BT_{peak})^2}{\sigma_{IR}} - 2\frac{(BT - BT_{peak})(VIS - VIS_{peak})}{\sigma_{IR}\sigma_{VIS}} + \frac{(VIS - VIS_{peak})^2}{\sigma_{VIS}}$$

where σ_{IR} and σ_{VIS} are the IR and VIS (VIS channels may be replaced with NIR channels) standard deviation respectively; VIS and IR are measurements in the solar and IR. The solar and infrared radiances can be a combination of various channels. The best solar channels to use are those for which the difference in reflectance between cloud and water is a maximum.

3.1.11 Detection of Cloud Shadows

The detection of cloud shadows is a problem that has not been addressed adequately in the literature. The following strategy is the first method we will employ to begin determining cloud shadows. The following discussion is only meant to provide an idea of the approach. Further work in this area has been initiated on this problem.

A 3 x 3 median filter first is applied to reduce noise in the image. It has the following desirable properties: 1) it does not affect the presence or position of the shadow edges, 2) no new brightness values are created, and 3) performance of the Laplace of Gaussian (LOG) zero crossing edge detection algorithm is improved.

Over oceans, histogram equalization of the MODIS channel 1 image is made first. The histogram equalization transform produces a histogram that is quasi-uniform on the average. It is based upon the discrete cumulative histogram with quantized brightness values. The dark values on the histogram equalized image are those due to cloud shadows.

Over land, the algorithm is more complex because shadows may fall upon both land surfaces of varying reflectances as well as water surfaces such as lakes, rivers and marshes. The application of a Laplacian filter to a Gaussian filter image is made first. This operation aids in the recognition of shadow and cloud regions. Edge locations are determined by the zero-crossings of the LOG-filtered image. Details are given in Berendes et al (1992). Many more edges are produced than just cloud and shadow ones. These are due to background variations and to noise.

To isolate the relevant shadow (or cloud) edge pixels, a thresholding procedure is used which is based on a restricted histogram, called the Max/Min histogram. This is constructed from the 3 x 3 neighborhood surrounding the potential edge pixels. The intention is to capture the modes of the transition pixels generating the edge elements. Generally, there are three distinctive peaks, due to 1) shadows, 2) background, and 3) clouds.

A weighted averaging of the peak values of the Max/Min histogram is used to determine the appropriate threshold between shadow and background (and between cloud and background). This is accomplished by taking into account the size of the distributions. The procedure is iterated to convergence. When water is present in the scene, then a four-mode Max/Min histogram is produced. The same iterative procedure is used to eliminate the background pixels, retaining both shadow and water pixels. The ancillary percent water data set is used to identify probable regions of water.

3.1.12 Automated Classification Methods

Artificial intelligence using fuzzy logic classifiers are applied from the outset to provide the context of the local region. Once the surface is known (water, solid sea ice or snow-covered land, broken sea ice, land,

patchy snow over land, frozen lakes and rivers) and once the basic cloud cover is known (stratus, stratocumulus, cumulus, cirrus, or multilayer), then the previously-defined tests are used at the pixel level. Somewhat different sets of the tests described previously are used for each of the various scenarios. Fuzzy logic classifier approaches are used to affect the highest accuracies in the retrievals.

The tests described so far are to one degree or another based upon thresholds. Texture is a powerful tool for defining the context of a region. We are considering texture computations over 15 km x 15 km subregions. To date, textures have not been invoked in most cloud mask algorithms; however, they are useful in regions which are uncertain. It is probably desirable to apply textures from the outset for difficult regions such as polar regions, coastlines, snow covered regions, and areas of variable topography. A texture-flag is set to inform the algorithm manager that texture is to be used.

Texture is often interpreted in the literature as a set of statistical measures of the spatial distribution of gray levels in an image. Here it is assumed that textural information is contained in the average spatial relationships that gray levels have with one another (Haralick et al. 1973). The gray level difference vector (GLDV) approach is based on the absolute differences between pairs of gray levels I and J found at a distance d apart at angle ϕ with a fixed direction. The GLDV difference-vector probability density function $P(m)_{d,\phi}$ is defined for m = I - J, where I and J are the corresponding gray levels having a value between 0 and 255. The gray level range may vary, but we will use 8-bit gray levels in our analysis. The density function $P(m)_{d,\phi}$ (henceforth P(m), where the dependence of P(m) on d and ϕ is implicitly assumed) is obtained by normalizing the GLDV difference vector by the total number of difference pairs. Once P(m) has been formed, textural measures are computed for each of the spectral channels (starting with the five AVHRR channels on MODIS ch 1, ch 2, ch 20, ch 31, ch 32) assuming a pixel separation distance of d = 1 and at an angle $\phi = 0°$ and 90°. The following textural features are computed for use in the classification system, and are calculated individually for each NxN pixel subarray.

Mean:

$$u = \sum m\, P(m)$$

Standard Deviation:

$$\sigma = [\, \sum (m-u)^2\, P(m)\,]^{1/2}$$

Contrast is a natural measure of the degree of spread in the gray levels. A small contrast value indicates high concentration of occurrences on the main diagonal and represents a coarse texture. Larger values of contrast indicate that the occurrences are spread out about the main diagonal and represents a finer structure.:

$$CON = \sum m^2\, P(m)$$

Angular second moment is a measure of homogeneity in the subscene. The measure is smallest when the gray levels are equally probable, and large values indicate that there are dominant gray levels present.

$$ASM = \sum [P(m)]^{\,2}$$

Entropy is a measure of disorder in the scene, and is largest for equally distributed gray levels and smallest when they are unequally distributed.

$$ENT = \sum P(m)\, \log[P(m)]$$

Local homogeneity is a measure of local similarity, and has a larger value for coarse textures than for finer textures.

$$HOM = \sum P(m)/(1 + m^2)$$

Cluster shade is a measure of the degree to which the outliers in the histogram favor one side or another of the mean.

$$CS = [\ \Sigma\ (m-u)^3\ P(m)\ ]/\sigma^3$$

Cluster prominence measures the effect of the outliers on the peak of the distribution.

$$CP = [\ \Sigma\ (m-u)^4\ P(m)\ ]/\sigma^4$$

These features are described by Chen et al. (1989) in greater detail. Plots of representative cloud texture measures as a function of pixel separation distance and angle are shown in Welch et al. (1989) and for a variety of ice and snow backgrounds in Welch et al. (1990).

The textures, along with the results from the previous tests, are then passed to an artificial intelligence (AI) classifier. It is a common misconception that AI techniques are operationally more cpu intensive. While AI techniques often do take longer to train, they are no more cpu intensive than are traditional approaches such as Maximum Likelihood. Indeed, many of these AI classifiers are more cpu efficient in the operational mode.

3.1.13 Quality Flags

Thresholds are never global. There are always exceptions. For example, the ch2/ch1 ratio test identifies cloud for values in the range $0.9 < ch2/ch1 < 1.1$. However, new analyses (McClain, 1993) suggest that the lower value may need to be lowered to about 0.8, at least for some cases. With the reflectance ratio test, it seems unrealistic to label a pixel with $ch2/ch1 = 1.1$ as cloudy, and a neighboring pixel with the ratio of 1.11 as non-cloudy. The same is true for the other tests using infrared radiances and spatial analysis. Rather, as one approaches the threshold limits, the certainty of the labeling becomes more and more uncertain, or "fuzzy". A quality flag must be assigned.

Therefore, it seems entirely reasonable to apply the highly deterministic fuzzy logic classifiers for pixels/regions which are labeled as uncertain by the previous tests. In a nutshell, fuzzy logic may be thought of as following the entire decision tree, keeping a running total of the uncertainty accumulated along each path. Instead of hard-and-fast thresholds, fuzzy membership functions are used. Then, at the termination of the decision tree, a "defuzzication" function is applied to the results. Uncertainty estimates of clear and cloudy at each pixel are the outcome. This fuzzy logic approach is being considered as a method of quantifying our confidence in the derived cloud mask for a given pixel.

3.1.14 Theoretical Discription of Aerosol Detection

Aerosols are a common occurrence in some regions of the globe, at least for part of the year. For example, dust is always present over large deserts during summer. Dust outbreaks transport dust from deserts, such as the Sahara, over the ocean, and therefore impact the cloud/aerosol mask.

The bulk transmittance of many aerosols displays a strong spectral dependence in the 8-12 micron region. For this reason, techniques have successfully employed temperature differences between the 11 and 12 micron channels of the AVHRR to detect aerosols (e.g., Prata 1989, Barton et al 1992). We have recently demonstrated that the tri-spectral technique is valuable for remote sensing of volcanic aerosols with visible optical depths greater than 0.2.

Mount Pinatubo erupted in June 1991. As no present single satellite instrument makes observations at all three wavelengths, we have composited observations from the HIRS/2 instruments flown on NOAA-10 and NOAA-11 satellites to demonstrate the technique. The NOAA-11 platform provides observations at 11 and 12

micron, while the HIRS/2 on the NOAA-10 provides observations at 8.6 and 11 micron. Clear sky observations with view angles less than 10° are averaged over 2° latitude by 3° longitude regions. To assess the impact of the Mt. Pinatubo aerosol, we compare August 1990 with observations made in August 1991.

Figure 7 is the tri-spectral plot of clear sky ocean scenes observed in August 1990 between 30°S-30°N. The slope indicated by the position of the points is a result of changing water vapor absorption, which in itself is very useful for inferring SST. Positive values of BT_{11}-BT_{12} result from stronger absorption at 12.5 microns, and the $BT_{8.6}$-BT_{11} negative values result from stronger absorption at 8.6 microns. The ellipse oriented along a least square linear regression between the variables, denotes the 95% probability that a point will fall within the enclosed region. This confidence ellipse is replicated on Figure 8 which depicts the post-Pinatubo tri-spectral observations for the month August 1991. Many points lie outside the 95% confidence ellipse generated with the 1990 observations. The departure is consistent with the effects of the aerosols from theoretical calculations. As the optical thickness of the aerosol increases, $BT_{8.6}$-BT_{11} and BT_{11}-BT_{12} decrease. While the change is in the same direction as an increase in water vapor for $BT_{8.6}$-BT_{11}, the change is opposite to that of increased water vapor for the BT_{11}-BT_{12} parameter. Thus, the three-channel technique may aid in separating the effects of water vapor from those of the aerosol. Note also that the differences from clear sky scenes caused by the presence of the volcanic aerosol is different from the spectral difference due to the presence of clouds.

Figure 9 depicts the index of refraction $m = n_r + i\, n_i$ as a function of wavelength for three elemental components common in soil derived aerosols. The real part of the index of refraction is an indication of the scattering properties, while the imaginary part is an indication of the absorption characteristics. The scattering and absorption properties will, of course, also depend on the particle size distribution; however, these diagrams are useful for illustrative purposes. The index of refraction of these elements is considerably different from ice or water, which suggests the three channel technique could be useful in separating heavy aerosol loading from clouds. Aerosol detection using solar reflected channels have also been demonstrated (Stowe et al. 1992, Kaufman and Sendra, 1988). Such applications are under consideration for the MODIS cloud mask

3.2 Practical Application of Cloud Detection Algorithms

3.2.1 Ancillary Data Set Requirements

A number of preprocessing steps will be made before the cloud masking algorithm is applied. First each pixel in the scene will be tagged as being land or water, and if land, a land/water percentage. Second, each land pixel will be designated as relatively flat, valley, isolated mountainous region, low mountains or hills, generally mountainous, or extremely rugged mountains. From the NOAA Snow Data Product each pixel will be designated as probably/probably not snow covered. Each land pixel will be classified as to its ecosystem, along with a more general ecosystem classification of urban, forest, woodland, grassland, shrubland, tundra, arid vegetation and highland vegetation. Ocean regions will be classified as water, coastline (including islands), possibility of isolated icebergs, marginal ice zone, and nearly solid sea ice (leads may be present). This requires ancillary data described below.

(1) The NAVY 10 minute database is a 1080 x 2160 array covering 180 degrees in latitude from north to south pole and 360 degrees in longitude. This database provides surface elevation, the percentage (an integer between 0 and 100) of water in the 10 minute box, and character type as shown in Table 3. Note that multiple characteristics are defined in this system; an example is code 4 = flat lake country or atoll.

Table 3. Earth surface character type and code.

Codes	Feature
0	salt or lake bed
1	flat or relatively flat
2	desert (or for high latitudes, glaciers or permanent ice)
3	marsh
4	lake country or atoll
5	major valleys or river beds
6	isolated mountains, ridge or peak
7	low mountains
8	mountainous
9	extremely rugged mountains
62	ocean

(2) The EPA Global Ecosystems (WE1.4D) Database also is a 1080 x 2160 byte array which contains 59 different ecosystems classes.

(3) The US NAVY/NOAA Sea Ice Product provides weekly reports of fractional ice coverage at spatial resolution of about 18 km.

(4) The NOAA Snow Data Product provides weekly report of snow cover at a spatial resolution of 150-200 km; snow is reported if the grid cell is more than 50% covered.

(5) The NMC 3-hour surface analyses of temperature and wind speed.

3.2.2 Implementation of the Cloud Mask Algorithms

3.2.2.1 Cloud Mask for Daylight Oceanic Areas

The procedures outlined here will be applied between 60° N and 60° S for oceanic regions and seasonally for large lakes (for which ice is very unlikely). Solar zenith angles are constrained to be less than 85°. The nighttime algorithm is used for sun glint areas. Sun glint occurs when the reflected sun angle lies between 0° and perhaps 36°. Reflectance of open water is strongly influenced by illumination and viewing geometry. Sun glint is also a function of surface wind. Pixels that pass the sun glint test but have little illumination due to high solar zenith angle ($>$ 85°) will be passed to the nighttime ocean algorithm.

The hierarchical approach we will use in the first version of the cloud mask has the following stages:

(1) Note pixels that have sun glint (possible effect on visible tests).

(2) Note pixels that have high solar zenith angle (possible effect on visible tests).

(3) Identify clear and cloudy pixels in a 5 km x 5 km region with spatial uniformity tests.
- Spatial IR uniformity test applied with ch 31 using Δ_{sc} = 3.5 K.
- Spatial reflectance uniformity test applied to ch 1 or 2.
- IR and vis 2-D histogram tests with chs 1 and 31

(4) Apply single fov masking tests in the following order:
- Reflectance 1 ratio test with ch2/ch1.
- Reflectance threshold test with ch 22
- Near infrared thin cirrus test with ch 26
- IR temperature threshold and difference tests with chs 20, 22, 29, 31, 32
- CO_2 test for high clouds with ch 35

(5) For regions in which the pixels are labeled as uncertain, automated classification techniques will be employed, such as the fuzzy logic classification system.

3.2.2.2 Cloud Mask for Daylight Land Areas

This portion of the algorithm is applied to land areas at latitudes from 60° N to 60° S, including islands. The hierarchy of cloud mask algorithm application is as follows.

(1) Check ecosystem (vegetation) map and land/water percentages data bases. Determine land/water percentage and vegetation for every pixel.

(2a) Compute sun glint angles for every pixel. Within the sun glint region the percent water database is examined (at 10 minute resolution). If water is present, then a flag is set indicating possible sun glint. Eliminate use of visible channels for sun glint pixels and apply nighttime algorithm to those pixels.

(2b) Over land pixels that are vegetated, compute scattering angle. If the scattering angle is close to 0°, there may be enhancements in the visible channel reflectances (hot spots).

(3) Check surface elevation, clear-sky radiance/temperature data base, and snow-cover data base.

(4) If the pixel or subregion is snow-covered, rugged terrain, coastline, and other special cases, pass imager data to automated classification algorithms.

(5) Apply spatial uniformity test to 5 km x 5 km regions.
- Spatial IR uniformity test applied with ch 31 using $\Delta_{sc} = 6.5$ K.
- Spatial reflectance uniformity test applied to ch 1 or 2.
- IR and vis 2-D histogram tests with chs 1 and 31

(6) Apply single fov masking tests in the following order:
- Reflectance 1 ratio test with ch2/ch1.
  this test will not be applied to desert regions
  apply to pixels labeled as cloud to reclassify as snow/ice; set snow flag
- Reflectance threshold test with ch 22
- Near infrared thin cirrus test with ch 26
- IR temperature threshold and difference tests with chs 20, 22, 29, 31, 32
- CO_2 test for high clouds with ch 35

(7) Check for consistency
- Spatial/temporal consistency tests
- IR clear-sky composite consistency test
- VIS/NIR clear-sky composite consistency test

(8) Pass uncertain pixels/subregions to automated classification algorithms.

The databases are examined for elevation characteristics and ecosystem type (see Figure 10). A separate database is examined for probability of snow (this will be contributed from the MODIS Science Team members who are

responsible for the snow cover product, Drs. V Salomonson and D. Hall). The snow probability index is set high if either the NOAA Snow Data Product is positive or if snow was indicated on the previous clear day. If the previous day was not clear, then local regions of the same ecosystem type are examined. If these regions also were cloudy on the previous day, then the pixel and its local regions are examined for two additional prior days. If these tests fail, then the snow flag is set to a low value. This test is seasonal; it is not run for tropical regions (except for regions of high elevation) or during summer months. NMC analyses also are examined. Prior days with surface temperatures > 10°C decrease the snow probability index values. On the other hand, during the late fall to early spring in the mid- to high-latitudes, cloud cover on the previous day coupled with surface temperatures in the NMC surface analysis increases the snow probability index. Note that this index has values between 0-100. As explained in Section 4.2.3, artificial intelligence and texture analysis are applied to regions which are uncertain. The fuzzy logic algorithm directly uses the snow probability index values.

3.2.2.3 Cloud Mask for Nighttime Ocean and Land Scenes

These algorithms are applied to all surface regions between 60° N and 60° S, for solar zenith angles greater than 85°, and for daytime pixels labeled as having sun glint, vegetation hot spots, or low illumination angles. Spatial coherence is used over oceans and over land areas of the same ecosystem.

(1) The initial step is to label each pixel with ecosystem, elevation, surface characteristics, snow/ice, and land/water percentage. If snow-covered, set flag.

(2) Retrieve short-term clear night (within last 72 hours) and radiance values for channels 21, 31, and 32. If there is no short-term clear night data available, use longer-term values. If the subregion is snow-covered, rugged terrain, coastline, or under the heading of other special cases, pass the subregion to automated classification algorithms. This is discussed further in section 3.2.2.5.

(3) Apply spatial uniformity to 5 km x 5 km regions, noting that the algorithm will be applied only to areas having the same ecosystem (e.g. water or ocean).

- Spatial IR uniformity test applied to ch 31
  where Δ_{sc} = 3.5 K for oceans and Δ_{sc} = 6.5 K for land.

(4) Apply single fov masking tests in the following order:

- IR temperature threshold and difference tests with chs 20, 22, 29, 31, 32
- CO_2 test for high clouds with ch 35
- mixed pixel analysis

(5) Apply consistency tests

- Spatial/temporal consistency test.
- IR clear-sky composite consistency test

(6) Pass uncertain pixels/subregions to automated classification algorithms.

3.2.2.4 Scene Classification for Daytime Polar Region Analysis

The daytime polar scene classification system currently separates 5 x 5 pixel subarrays into the following classes:

(1) Water
(2) Solid sea ice or snow-covered land
(3) Broken sea ice
(4) Snow-covered mountains (or regions of high relief)
(5) Stratus-type clouds over water
(6) Stratus-type cloud over ice
(7) Cirrus clouds over ice
(8) Cumulus clouds over water
(9) Multilayer cloudiness
(10) Non-snow-covered land

These classes need to be expanded somewhat to include, for example, cirrus clouds over water. To date, high accuracies are achieved for pure classes. However, additional work is in progress to extend the classes and to include a broader range of textural measures.

This algorithm is applied poleward of 60° N and 60° S and is based upon Ebert (1987, 1989), Key and Barry (1989), Welch et al. (1992) and Tovinkere et al. (1993). The following ten spectral and textural measures are defined for 5 km x 5 km and 15 km x 15 km regions respecitively.

(1) ch1-ch2
(2) Low ch22
(3) ch22/ch1
(4) Mean ASM ch22
(5) Mean ch1
(6) Max Ent ch1
(7) Mean ch31
(8) Max Ent ch31
(9) ch31-ch 32
(10) ch31-ch 27

Measure 1. ch1-ch2: The reflectance difference between chs 1 and 2. This measure is positive for classes with snow and ice surfaces and negative for land. The reflectance difference $r_{.66}$-$r_{.87}$ tends to have a positive value for the cloud classes and for water and snow and negative for land.

Measure 2. Low ch22: This is the percentage of pixels in ch 22 that have a reflectance, $r_{3.9}$, less than 10%. This is the greatest for water and snow and least for stratus and stratocumulus cloudiness.

Measure 3. ch22/ch1: The mean reflectances values of chs 1 and 22 are computed, and the ratio, $r_{.66}/r_{3.9}$, is calculated using these values. This value is low for ice covered surfaces and cirrus cloudiness.

Measure 4. Mean ASM ch22: Angular second moment of ch 22. This textural feature is a measure of homogeneity in the scene. This measure is smallest when all the gray levels occur with equal probability.

Measure 5. Mean ch1: This is the mean reflectance of ch 1, $r_{.66}$, which must be greater than a threshold value for clouds.

Measure 6. Max Ent ch1: This is a measure of disorder in the scene. The entropy measure is calculated from ch 1. It has low values for water, solid sea ice, and land.

Measure 7. Mean ch31. This is the mean brightness temperature computed from channel 31, BT_{11}, which must be colder than a threshold value for clouds.

Measure 8. Max Ent ch31: This is the entropy measure of the region in ch 31. Max Ent ch31 has low values for classes which display distinct scales of organization and relatively uniform temperatures.

Measure 9. ch31-ch32: The brightness temperature difference between chs 31 and 32. Surface inversion confusion with cirrus cloud can be mitigated by testing BT_{11}-BT_{12}.

Measure 10. ch31-ch27: The brightness temperature difference between chs 31 and 27. BT_{11}-$BT_{6.7}$ shows large negative difference over the Antarctic Plateau winter which may be indicative of clear sky and the existence of a strong surface inversion and thus clear skies.

The means and standard deviations are calculated for the complete training data set. These features are defined for daylight ($\theta_o < 85°$). Also, the pixel arrays are defined over a single ecosystem type. The pixel array covering 5 km x 5 km may be modified to suit individual regions, by altering the size of the array to be larger or smaller and by altering the shape of the region as necessary. If a single ecosystem type cannot be defined for a given region, then a broader categorization of forest, tundra, etc., is used.

The NAVY weekly 18 km sea ice product is utilized to define the marginal ice zone. Oceanic regions within 100 km of the ice edge are labeled as probably broken sea ice. Regions further poleward are labeled with distance as more and more probable of being solid sea ice. Regions in the opposite direction are labeled with distance as less and less probable of being broken sea ice.

The NMC surface temperature analysis is used for consistency checks. For example, warm surface temperatures (> 273 K) indicate ice melt, probable melt ponds, and lower ice/snow reflectivities. On the other hand, very low surface temperatures generally are consistent with the lack of open water and with higher surface reflectivities. Such cold surface temperatures also mean that the various thermal tests need to be applied over more restricted domains.

3.2.2.5 Short-term and Long-term Clear-Sky Composite Maps

Composite Maps have been found to be useful by ISSCP. The MODIS cloud mask will expand upon this concept as useful, noting that the advantages of higher spatial resolution and more spectral bands will change the application and the need. The ISCCP developed clear-sky reflectance and temperature composites to detect clouds over a given 32-km square area by comparing the pixel radiances to the clear-sky composite values with some added thresholds (Rossow and Garder 1993). These composites are based on the observation that variations in VIS clear reflectances usually are smaller in time than in space, especially over land. Variations of surface VIS reflectances generally are smaller than variations of cloud reflectances. Therefore, it is assumed that the characteristic shape of the darker part of the VIS radiance distribution is at most weakly dependent upon surface type (Seze and Rossow, 1991a, b). The minimum reflectance value for channel 1 is used to estimate clear values. Corrections to the minimum values are inferred from the shapes of the visible reflectance distribution associated with different surface types.

Rossow and Garder (1993) classify the surface into nine types depending on the time scale and magnitude of the reflectance variations (see Tables 4 and 5). The clear sky reflectance values for land and ocean regions whose surface characteristics vary the most rapidly are estimated using short-term values of ρ_{min} such that $\rho_{cs} = \rho_{min}(ST) + DEL2$. Sparsely vegetated surfaces generally exhibit more spatial variability than heavily vegetated surfaces (cf. Matthews and Rossow, 1987), but are also generally less cloudy. Sparsely vegetated arid regions generally exhibit more spatial variability (Matthews and Rossow, 1987) and are less cloudy. For these, $\rho_{cs} = \rho_{min}(LT) + DEL2$. Vegetated areas show less small scale spatial variability. They also tend to be more uniform from one geographic location to another. For vegetated regions, the clear-sky reflectance is determined by first calculating $\rho_{cs} = \rho_{min}(ST) + DEL2$. Then the individual pixel reflectance values within each latitude zone are

compared to the distribution of ρ_{cs} values for the same ecosystem type; they are required to be within DEL1 of the distribution mode value, ρ_{mode}.

Similar assumptions are used for the determination of clear sky temperature fields. The time scales of IR variability for different classes and the associated ISCCP thresholds are shown in Tables 6 and 7.

Table 4. Time scales of variability for different surface types for visible/near infrared channels.

VIS classes	Short Term	Long Term
Ocean	-	30 days
Lakes	-	15 days
Polar ocean (open water)	-	15 days
Ice-covered water	5 days	-
Forests, woodlands, shrublands	-	30 days
Grasslands, tundra	-	30 days
Arid vegetation, deserts	-	30 days
Polar land (snow free)	-	15 days
Snow- or ice-covered land	5 days	-

Table 5. Values used in VIS/NIR clear-sky composite logic (after Rossow and Garder, 1993). Values are in percent scaled radiances.

VIS surface types	DEL1	DEL2
Ocean, Lakes, Polar ocean (open)	3.0	1.5
Ice-covered water	-	5.0
Forests,woodlands,shrubland	6.0	3.5
Grasslands, tundra	-	3.5
Arid vegetation, deserts	-	3.5
Polar Land (snow free)	-	3.5
Snow- or Ice-covered land	-	5.0

Table 6. Time scales of variability for different surface types for IR channels.

IR classes	Short Term	Long Term
Open ocean	15 days	30 days
Near-coastal ocean and lakes	5 days	15 days
Polar seas and ice covered water	5 days	15 days
Land	5 days	15 days
High and rough topography land	5 days	15 days
Ice- or snow-covered land	5 days	15 days

Table 7. Test values used in IR composite logic (after Rossow and Garder, 1993). IR values are in Kelvins.

IR surface types	DEL1	DEL2	DEL3
ocean	2.0	2.0	2.5
near-coastal ocean, lakes	3.0	3.0	4.0
ice-covered water	3.0	3.0	4.0
land	6.0	5.0	8.0
high or rough topography	9.0	7.0	11.0
ice or snow-covered land	9.0	7.0	11.0

One of the primary difficulties in using the ISCCP approach as currently formulated is the angular dependence of clear-sky reflectance. Although cross-track scanning Sun-synchronous satellites such as the NOAA-AVHRR repeat the angular viewing conditions on a regular 11-day cycle, the solar zenith angle slowly varies and the cloudiness conditions may prevent the determination of clear-sky reflectance at some points in the 11-day cycle. The ISCCP relies on an empirical bidirectional reflectance model for clear-sky ocean (Minnis and Harrison, 1984a) reflectance. Thus, over ocean, the angular problems are minimized. Over land, the ISCCP assumes isotropic clear-sky reflectance, although it has been established that the anisotropy of land scenes is significant (e.g., Kriebel, 1978; Tarpley, 1979; Minnis and Harrison, 1984c; Suttles et al., 1988). For $\theta o < 85°$, the vegetated land clear-sky anisotropic reflectance factor $R(\kappa, \theta o, \theta, \phi)$, where κ is a surface type, can vary from 0.6 to 1.6 (e.g., Suttles et al., 1988) for $\theta < 70°$. Thus, there is the potential for clear-sky reflectance errors as great as 300% if one assumes that the measurement taken at a particular set of viewing conditions represents the reflectance at all viewing angles for a given value of θo. Systematic changes of albedo with θo are also not considered for land surfaces. The reflectance anisotropy over snow and desert scenes is generally not as great as that over vegetated surfaces, but the absolute changes in reflectance are as great because of the higher albedos over these surfaces.

The MODIS processing will composite a set of global clear-sky radiances for ascending and descending nodes matched to the Navy 10 minute database. Compositing of clear-sky radiance maps from MODIS data will be done on time-scales suggested by ISCCP (tables 4 and 6). ISCCP thresholds (Tables 5 and 7) along with CLAVR clear-sky radiance analysis (Stowe et al. 1991) will be used as guidance for the MODIS clear-sky composite map development.

3.2.3 Numerical Programming Considerations

Versions of the indicated algorithms are currently be used on HIRS and AVHRR data. It is difficult to make an accurate prediction of the total lines of code required to produce the presently proposed cloud mask. Our estimate is based on (1) a real-time program that accesses and collocates AVHRR and HIRS/2 data in real time and applies some of the clear/cloud tests presently proposed, and (2) a pattern recognition technique to classify cloud fields applied to AVHRR and HIRS data.

Estimates of the processing required for the MODIS cloud mask are made by using the HIRS/AVHRR cloud detection algorithm. The cpu time required for HIRS/AVHRR GAC (4 km resolution) global coverage (view angles out to 30°) is 84 minutes. To produce a MODIS Cloud Mask product at 1 km resolution is estimated to require a factor of 100 increase over the HIRS/AVHRR processing, i.e. 8400 minutes. This estimate accommodates the increase in the number of spectral channels and the increase in spatial resolution. The current HIRS/AVHRR cloud work is being done on an IBM RISC 6000.

3.2.4 Quality Control

Quality control is also difficult to specify. The present approach is to base quality control on the number of different clear sky tests that an individual FOV passes. Under certain conditions, certain methods will be more reliable than others and this will be considered in the quality control flag. Application of fuzzy logic techniques are also under consideration as a provider of quality control flags.

The MODIS cloud mask algorithms should be developed using two data sets (1) MAS data for obvious reasons (2) collocated AVHRR and HIRS/2 data. The latter set gives global coverage of many of the MODIS channels though with larger FOVs. Thus many applications, though not all, developed with the MAS can be tested with this global data set to determine what type of global variability is to be expected.

Final validation will not occur until some MODIS data is actually available. While a version of the cloud/aerosol mask will be available at launch, it is expected that extensive verification will require analysis of individual scenes.

4.0 Complete List of References

Ackerman, S. A., W. L. Smith and H. E. Revercomb, 1990: The 27-28 October 1986 FIRE IFO cirrus case study: spectral properties of cirrus clouds in the 8-12 micron window. Mon. Wea. Rev., 118, 2377-2388.

Allen, R. C., Jr., P. A. Durkee and C. H. Wash, 1990: Snow/cloud discrimination with multispectral satellite measurements. J. Appl. Met., 29, 994-1004.

Arking, A., and J. D. Childs, 1985: Retrieval of cloud cover parameters from multispectral satellite images. J. Clim. Appl. Met., 24, 322-333.

Berendes, T., S. K. Sengupta, R. M. Welch, B. A. Wielicki, and M. Navar, 1992: Cumulus cloud base height estimation from high spatial resolution data: A Hough transform approach. IEEE Trans. Geosci. Remote Sens., 30, 430-443.

Booth, A. L., 1973: Objective cloud type classification using visual and infrared satellite data. 3rd Conference on Probability and Statistics in the Atmospheric Sciences. Am. Meteor. Soc., Boulder, CO.

Brooks, D. R., E. F. Harrison, P. Minnis, J. T. Suttles, and R. S. Kandel, 1986: Development of algorithms for understanding the temporal variability of the earth's radiation balance. Rev. Geophys. 24, 422-438.

Chen, D. W., S. K. Sengupta, and R. M. Welch, Cloud field classification based upon high spatial resolution textural features, Part 2, Simplified vector approaches, J. Geophys. Res., 94, 14,749-14,765, 1989.

Coakley, J. A, 1987: A dynamic threshold method for obtaining cloud cover from satellite imagery data. J. Geophys. Res., 92, 3985-3990.

Coakley, J. A. and F. P. Bretherton, 1982: Cloud cover from high-resolution scanner data: Detecting and allowing for partially filled fields of view. J. Geophys. Res., 87, 4917-4932.

Derrien, M., B. Fraki, L. Harang, H. Legleau, A. Noyalet, D. Pochic, and A. Sairouni, 1993: Automatic cloud detection applied to NOAA-11 AVHRR imagery. Remote Sens. Environ, 46, 246-267.

Deschamps, P. Y. and T. Phulpin, 1979: Atmospheric correction of infrared measurements of sea surface temperature using channels at 3.7, 11, and 12 microns. Boundary Layer Meteor., 18, 131-143.

Ebert, E. E., 1987: A pattern-recognition technique for distinguishing surface and cloud types in the polar-regions. J. Clim. Appl. Meteor., 26, 1412-1427.

Ebert, E., 1989: Analysis of polar clouds from satellite imagery using pattern recognition and a statistical cloud analysis scheme. J. Appl. Meteor., 28, 382-399.

Gao, B.-C., A. F. H. Goetz, and W. J. Wiscombe, 1993: Cirrus cloud detection from airborne imaging spectrometer data using the 1.38 micron water vapor band. Geophys. Res. Letter, 20, no. 4, 301-304.

Garand, L., 1988: Automated recognition of oceanic cloud patterns. Part I: Methodology and application to cloud climatology. J. Climate, 1, 20-39.

Giarratano, J. and G. Riley, 1989: Expert Systems: Principle+s and Programming, 632 pp., PWS-KENT Publishing Company, Boston, 1989.

Gutman, G., D. Tarpley, and G. Ohring, 1987: Cloud screening for determination of land surface characterisitics in a reduced resolution satellite data set. Int. J. Remote Sensing, 8, 859-870.

Haralick, R. M., K. S. Shammugam, and I. Dinstein, 1973: Textural features for image classification. IEEE Trans. On Systems, Man, and Cybernetics, Vol. SMC-3, No. 6, 610-621.

Hecht-Nielsen, R., 1990: Neurocomputing. Addison-Wesley, Reading, MA, 430 pp.

Inoue, T., 1987: A cloud type classification with NOAA 7 split window measurements. J. Geophys. Res., 92, 3991-4000.

Inoue, T., 1989: Features of clouds over the Tropical Pacific during the Northern Hemispheric winter derived from split window measurements. J. Meter. Soc. Japan, 67, 621-637.

Jacobowitz, H. J., 1970: Emission scattering and absorption of radiation in cirrus clouds. Ph.D. thesis, Massachusetts Institute of Technology, 181 pp.

Kaufman, Y. J., 1987: Satellite sensing of aerosol absorption. J. Geophys. Res., 92, 4307-4317.

Kaufman, Y. J., and C. Sendra, 1988: Algorithm for atmospheric corrections of visible and near IR satellite imagery. Int. J. Remote Sens., 9, 1357-1381.

Kaufman, Y. J., and T. Nakajima, 1993: Effect of Amazon smoke on cloud microphysics and albedo - analysis from satellite imagery. J. Appl. Met., 32, 729-744.

Key, J. and R. G. Barry, 1989: Cloud cover analysis with Arctic AVHRR data. 1. Cloud detection. J. Geophys. Res., 94, 8521-8535.

King, M. D., Y. J. Kaufman, W. P. Menzel and D. Tanre, 1992: Remote sensing of cloud, aerosol, and water vapor properties from the Moderate Resolution Imaging Spectrometer (MODIS). IEEE Trans. Geosci. Remote Sensing, 30, 2-27.

Kriebel, K. T., 1978: Measured spectral bidirectional reflection properties of four vegetated surfaces. Appl. Opt., 17, 253-259.

Lee, J., R. Weger, S. K. Sengupta, and R. M. Welch, 1990: A neural network approach to cloud classification. IEEE Trans. Geosci. and Remote Sens., 28, 846-855.

Luger, G. F. and W. A. Stubblefield, 1989: Artificial Intelligence and the Design of Expert Systems, 600 pp., The Benjamin Cummings Publishing Company, Inc., 1989.

Matthews, E. and W. B. Rossow, 1987: Regional and seasonal variations of surface reflectance from satellite observations at 0.6 mm. J. Climate Appl. Meteor., 26, 170-202.

McClain, E. P., 1993: Evaluation of CLAVR Phase-I algorithm performance: Final Report, U. S. Department of Commerce/NOAA/NESDIS, Report 40-AANE-201-424.

McMillin, L. M., and C. Dean, 1982: Evaluation of a new operational technique for porducing clear radainces. J. Appl. Meteor., 12, 1005-1014.

Menzel, W. P. and K. I. Strabala, 1989: Preliminary report on the demonstration of the VAS CO_2 cloud parameters (cover, height, and amount) in support of the Automated Surface Observing System (ASOS). NOAA Tech Memo NESDIS 29.

Menzel, W. P., D. P. Wylie, and K. I. Strabala, 1992: Seasonal and Diurnal Changes in Cirrus Clouds as seen in Four Years of Observations with the VAS. J. Appl. Meteor., 31, 370-385.

Menzel, W. P., D. P. Wylie, and K. I. Strabala, 1993: Trends in Global Cirrus Inferred from Four Years of HIRS Data. Technical Proceedings of the Seventh International TOVS Study Conference held 10-16 February in Igls, Austria.

Minnis, P. and E. F. Harrison, 1984a: Diurnal variability of regional cloud and clear sky radiative parameters derived from GOES data. Part I: Analysis method. J. Climate Appl. Meteor., 23, 993-1011.

Minnis, P. and E. F. Harrison, 1984b: Diurnal variability of regional cloud and clear sky radiative parameters derived from GOES data. Part II: November 1978 cloud distributions. J. Climate Appl. Meteor., 23, 1012-1031.

Minnis, P., and E. F. Harrison, 1984c: Diurnal variability of regional cloud and clear-sky radiative parameters derived from GOES data, Part III: November 1978 radiative parameters. J. Clim. Appl. Meteor., 23, 1032-1051.

Minnis, P., E. F. Harrison and G. G. Gibson, 1987: Cloud cover over the eastern equatorial Pacific derived from July 1983 ISCCP data using a hybrid bispectral threshold method. J. Geophys. Res., 92, 4051-4073.

Parol, F. J., C. Buriez, G. Brogniez and Y. Fouquart, 1991: Information content of AVHRR Channels 4 and 5 with respect to the effective radius of cirrus cloud particles. J. Appl. Meteor., 30, 973-984.

Phulpin, T., M. Derrien, and A. Baird, 1983: A two-dimensional histogram procedure to analyze cloud cover from NOAA satellite high resolution imagery. J. Clim. Appl. Meteor., 22, 1332-1345.

Prabhakara, C., J.-M. Yoo, D. P. Kratz, and G. Dalu, 1993: Boundary layer stratus clouds: inferred from satellite infrared spectral measurements over oceans. J. Quant. Spectrosc. Radiat. Transfer, 49, 599-607.

Rao, C. R. N., L. L. Stowe, and L. L. McClain, 1989: Remote sensing of aerosol over the oceans using AVHRR data: theory, practice, and applications. Int. J. Remote Sensing, 10, 743-749.

Raschke, E., P. Bauer, and H. J. Lutz, 1992: Remote sensing of clouds and surface radiation budget over polar regions. Int J. Remote Sensing, 13, 13-22.

Reutter, H. , F. -S. Olesen, and H. Fischer, 1994: Distribution of the brightness temperature of land surfaces determined from AVHRR data. Int. J. Remote Sensing, 15, 95-104.

Rossow, W. B., 1989: Measuring cloud properties from space. A review. J. Climate, 2, 201-213.

Rossow, W. B., and A. A. Lacis, 1990: Global and seasonal cloud variations from satellite radiance measurements. Part II: Cloud properties and radiative effects. J. Clim., in press.

Rossow, W. B. and L. C. Garder, 1993: Cloud detection using satellite measurements of infrared and visible radiances for ISCCP. J. Climate, 6, 2341-2369.

Rumelhart, D. E., G. Hinton, and R. Williams, 1986: Learning internal representations by error propagation. In Parallel Distributed Processing: Exploration in the Microstructure of Cognition. D. Rumelhart and J. McClelland (eds.), MIT Press, pp. 318-362.

Sakellariou, N. K., H. G. Leighton, and Z. Li, 1993: Identifcation of clear and cloudy pixels at high latitudes from AVHRR radiances. Int. J. Remote Sensing, 14, 2005-2024.

Saunders, R. W., 1986: An automated scheme for the removal of cloud contamination from AVHRR radiances over western Europe. Int. J. Remote Sensing., 7, 867-886.

Saunders, R. W. and K. T. Kriebel, 1988: An improved method for detecting clear sky and cloudy radiances from AVHRR data. Int. J. Remote Sens., 9, 123-150.

Seze, G. and M. Desbois, 1987: Cloud cover analysis from satellite imagery using spatial and temporal characteristics of the data. J. Climate Appl. Meteor., 26, 287-303.

Seze, G., and W. B. Rossow, 1991a: Time-cumulated visible and infrared radiance histograms used as descriptors of surface and cloud variations. Int. J. Remote Sens., 12, 877-920.

Seze, G., and W. B. Rossow, 1991b: Effects of satellite data resolution on measuring the space-time variations of surfaces and clouds. Int. J. Remote Sens., 12, 921-952.

Simpson, J. J., and C. Humphrey, 1990: An automated cloud screening algorithm for daytime advanced very high resolution radiometer imagery. Jour. Geo. Res., 95, 13459-13481.

Stevens, G. L., 1990: On the Relationship between Water Vapor over the Oceans and Sea Surface Temperature. J. Clim., 3, 634-645.

Stowe, L. L., E. P. McClain, R. Carey, P. Pellegrino, G. Gutman, P. Davis, C. Long, and S. Hart, 1991: Global distribution of cloud cover derived from NOAA/AVHRR operational satellite data. Adv. Space Res., 11, 51-54.

Stowe, L. L., R. M. Carey, and P. Pellegrino, 1992: Monitoring the Mt. Pinatubo aerosol layer with NOAA/11 AVHRR data. Geo. Res. Letters, 19, 159-162

Stowe, L. L., S. K. Vemury, and A. V. Rao, 1994: AVHRR clear sky radiation data sets at NOAA/NESDIS. Adv. Space Res., 14, 113-116.

Strabala, K. I., S. A. Ackerman, and W. P. Menzel, 1994: Cloud Properties Inferred from 8-12μm Data. J. Appl. Meteor., 33, 212-229.

Susskind, J., D. Reuter, and M. T. Chahine, 1987: Cloud fields retrieved from analysis of HIRS/MSU sounding data. J. Geophys. Res., 92, 4035-4050.

Suttles, J. T., R. N. Green, P. Minnis, G. L. Smith, W. F. Staylor, B.A. Wielicki, I. J. Walker, D. F. Young, V. R. Taylor, and L. L. Stowe, 1988: Angular radiation models for Earth-atmosphere system: Volume I - Shortwave radiation. NASA RP 1184, 144 pp.

Takano, Y., K. N. Liou and P. Minnis, 1992: The effects of small ice crystals on cirrus infrared radiative properties. J. Atmos. Sci., 49, 1487-1493.

Tanre, D., P.Y. Deschamps, C. Devaux, and M. Herman, 1988: Estimation of Saharan aerosol optical thicknesses from blurring effects in Thematic Mapper data. J. Geophys. Res, 93, 15955-15964.

Tarpley, J. D., 1979: Estimating incident solar radiation at the surface from geostationary satellite data. J. Appl. Meteor., 18, 1172-1181.

Tovinkere, V. R., M. Penaloza, A. Logar, J. Lee, R. C. Weger, T. A. Berendes, and R. M. Welch, 1993: An intercomparison of artificial intelligence approaches for polar scene identification, J. Geophys. Res., 98, 5001-5016.

Vidal, A., 1991: Atmospheric and emissivity correction of land surface temperature measured from satellite using ground measurements or satellite data. Int. J. Remote Sensing, 12, 2449-2460.

Warren, S. G., 1984: Optical constants of ice from the ultraviolet to the microwave. Appl. Optics, 23, 1206-1225.

Welch, R. M., S. K. Sengupta, A. K. Goroch, P. Rabindra, N. Rangaraj, and M. S. Navar, 1992: Polar cloud and surface classification using AVHRR imagery: An intercomparison of methods, J. Appl. Meterol., 31, 405-420.

Welch, R. M., K. S. Kuo, S. L. Sengupta, 1990: Cloud and surface textural features in polar regions. IEEE Trans. Geosci., and Remote Sens., 28, 520-528.

Welch, R. M., M. S. Navar, and S. K. Sengupta, 1989: The effect of spatial resolution upon texture-based cloud field classifications. J. Geophys. Res. 94, 14767-14781.

Wielicki, B. A., and J. A. Coakley, 1981: Cloud retrieval using infrared sounder data: Error analysis. J. Appl. Meteor., 20, 157-169.

Wylie, D. P., and W. P. Menzel, 1989: Two years of cloud cover statistics using VAS. J. Clim. Appl. Meteor., 2, 380-392.

Wylie, D. P., W. P. Menzel, H. M. Woolf, and K. I. Strabala, 1994: Four Years of Global Cirrus Cloud Statistics Using HIRS. accepted by J. Clim.

Yamanouchi, T., K. Suzuki, and S. Kawaguci, 1987: Detection of clouds in Antarctica from infrared multispectral data of AVHRR. J. Meteor. Soc. Japan, 65, 949-962.

5.0 Figures

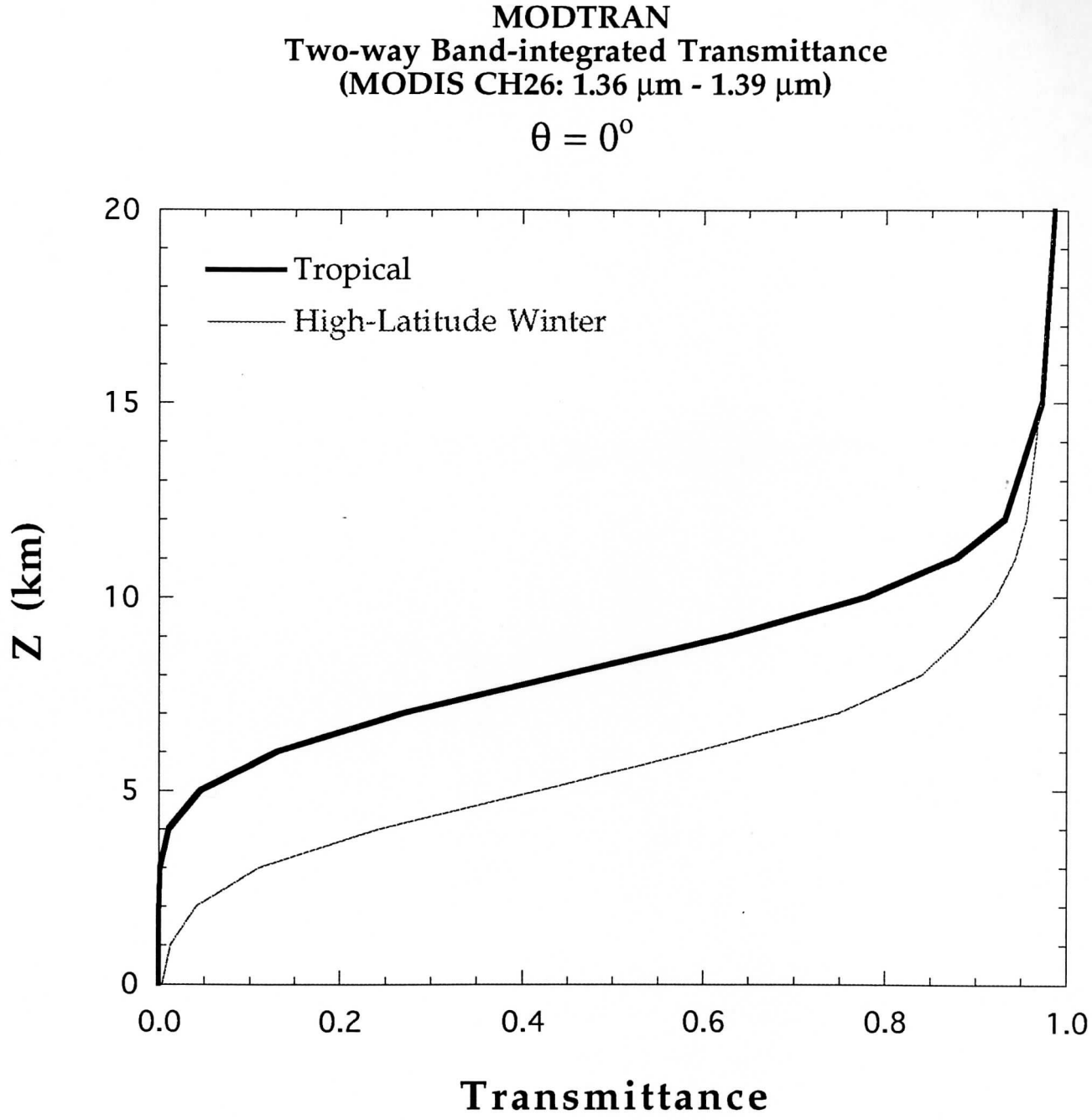

Figure 1. Two way clear sky transmittance for MODIS channel 26 (1.38 microns) for two sample atmospheres from Lowtran 7. Incoming path (top of atmosphere to level Z) has 45° zenith angle; outgoing path (level Z to top of atmosphere) has 0° zenith angle.

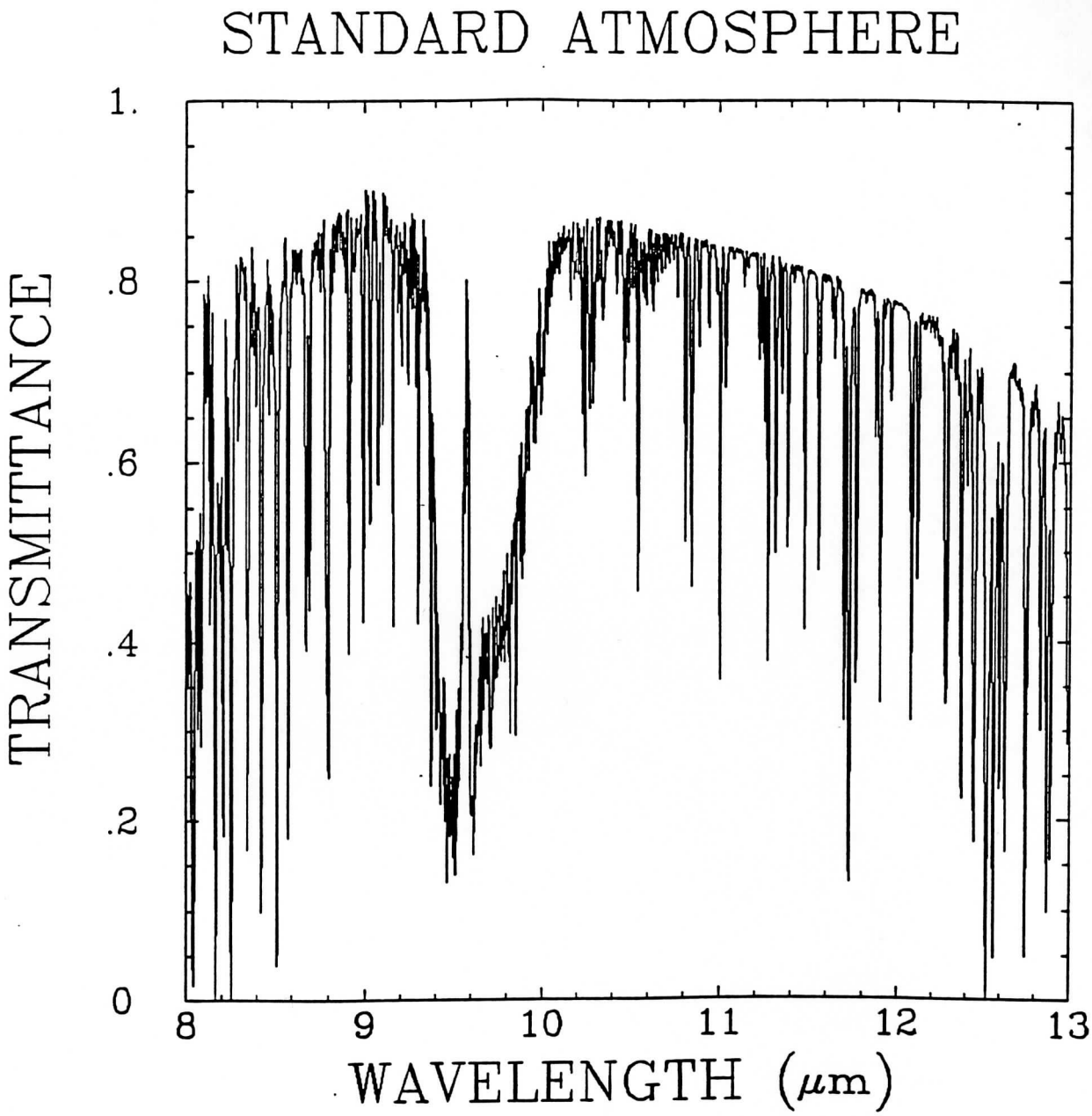

Figure 2. HIS (High resolution Interferometer Sounder) total transmittance spectra for a standard atmosphere across the 8-13μm window.

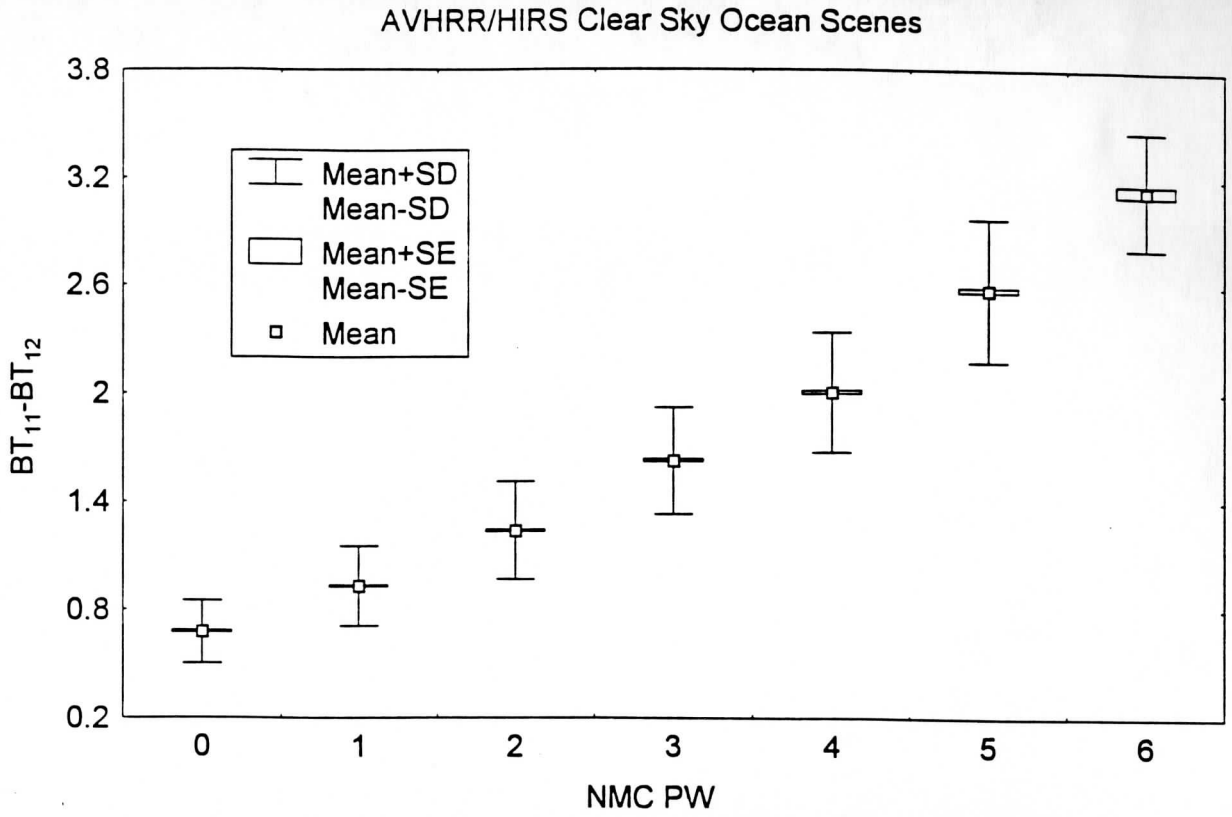

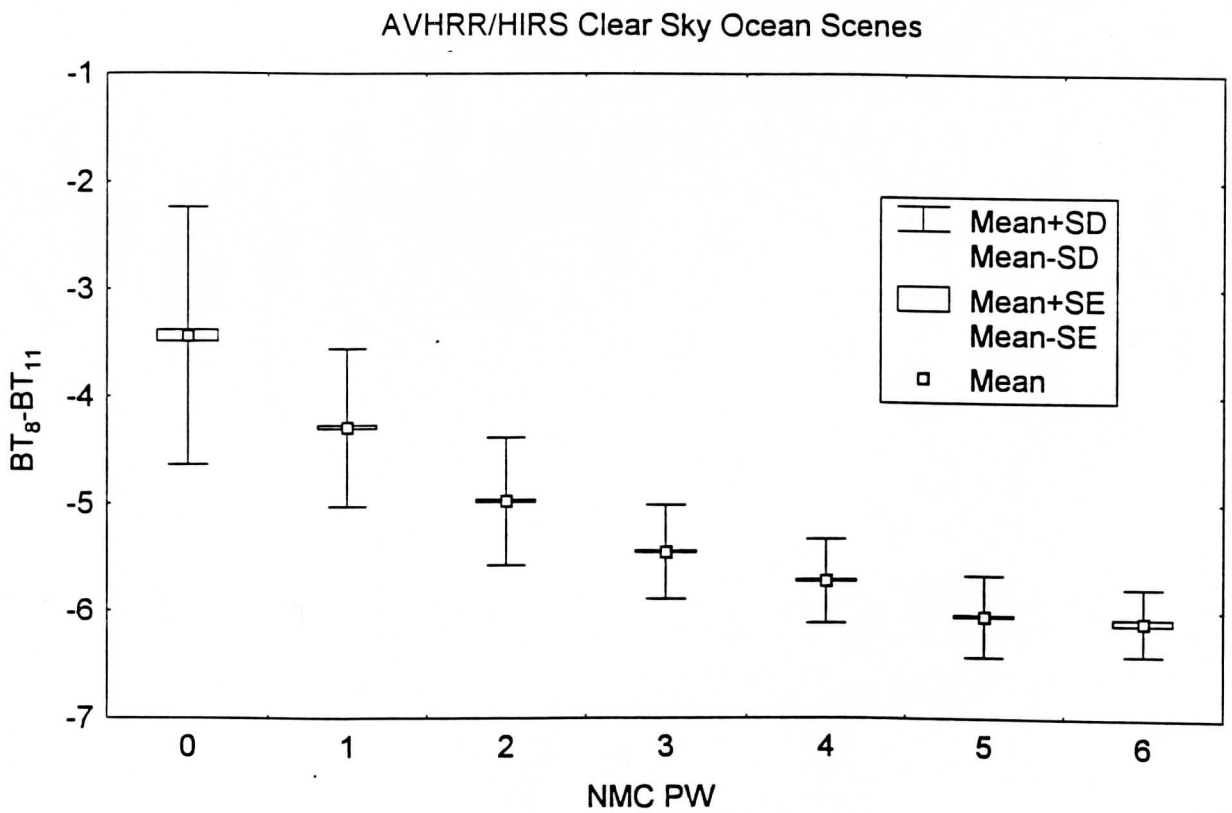

Figure 3. Observed AVHRR 11-12 micron (top panel) and collocated HIRS 8-11 micron (bottom panel) brightness temperature differences versus NMC total column PW for one month (January 1994) of clear ocean scenes.

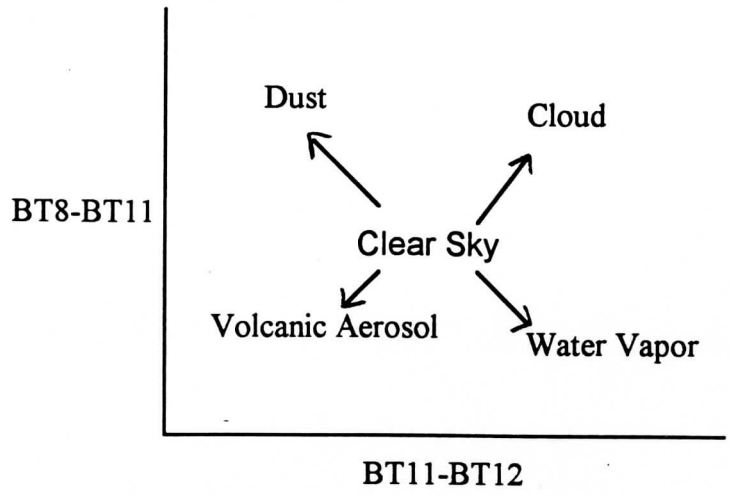

Figure 4. Schematic diagram of the effects of different atmospheric constituents on the brightness temperature differences between 11 and 12 micron (BT_{11}-BT_{12}) and 8.6 and 11 micron ($BT_{8.6}$-BT_{11}).

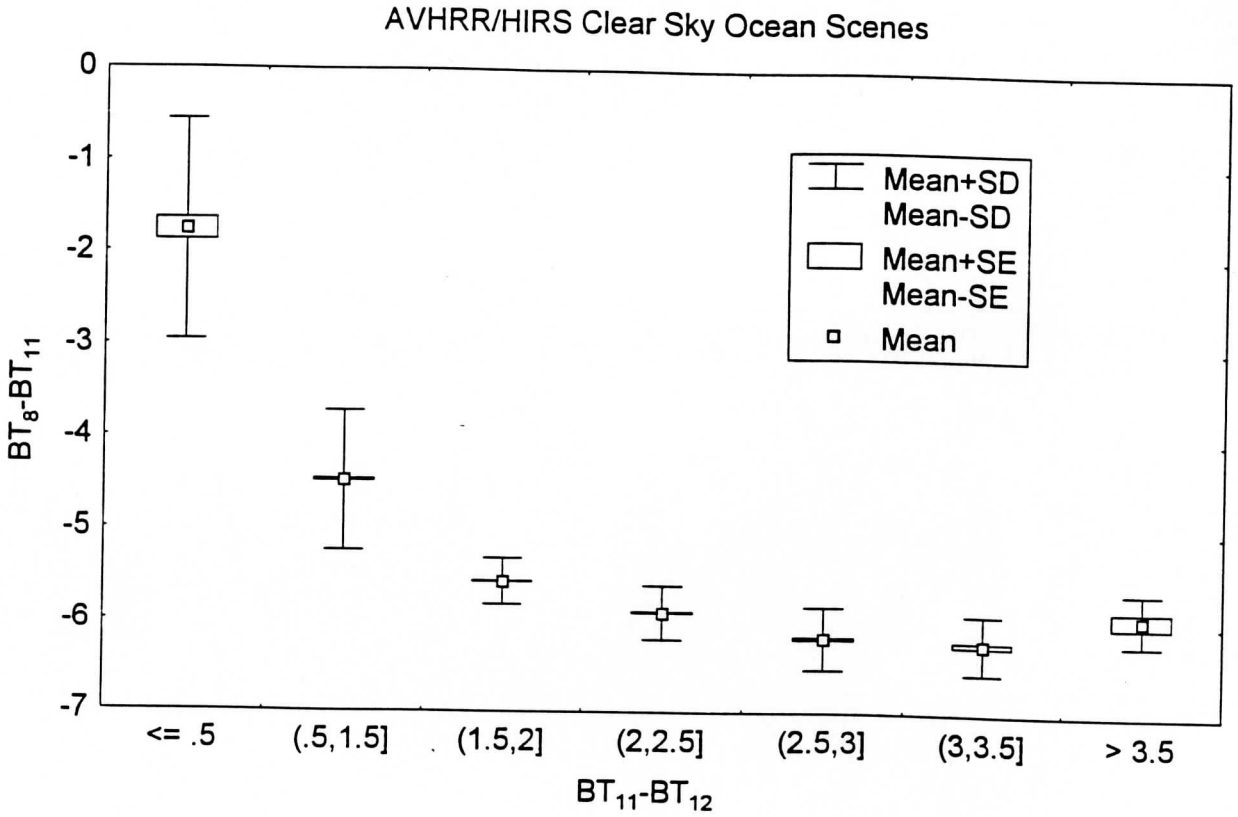

Figure 5. Scatter diagram of collocated HIRS 8-11 micron versus AVHRR 11-12 micron brightness temperature differences for one month (January 1994) of clear ocean scenes. From Figure 3 it is apparent that as atmospheric moisture increases, the 11-12 micron brightness temperature difference increases while the 8-11 micron brightness temperature difference decreases.

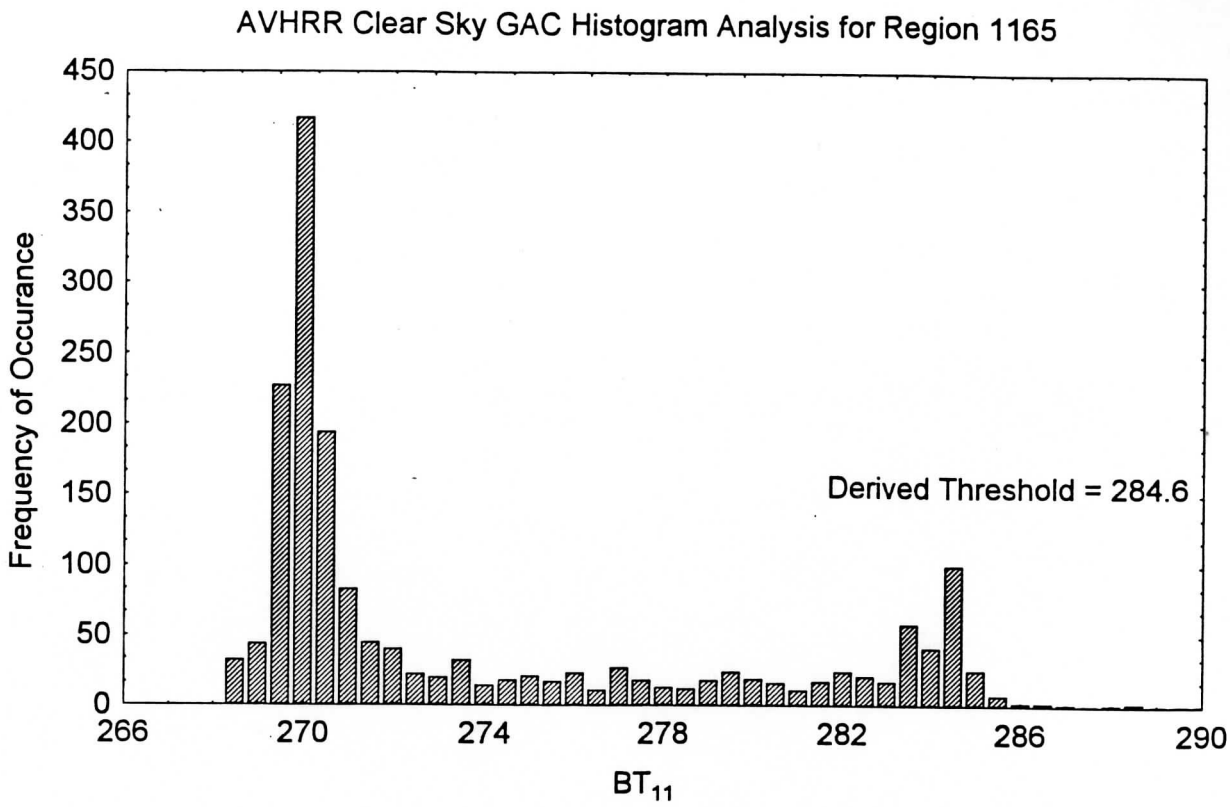

Figure 6. Example of infrared histogram analysis technique using AVHRR GAC data for a 2.5° x 2.5° ocean region. The derived clear-sky BT_{11} threshold is 284.6 K.

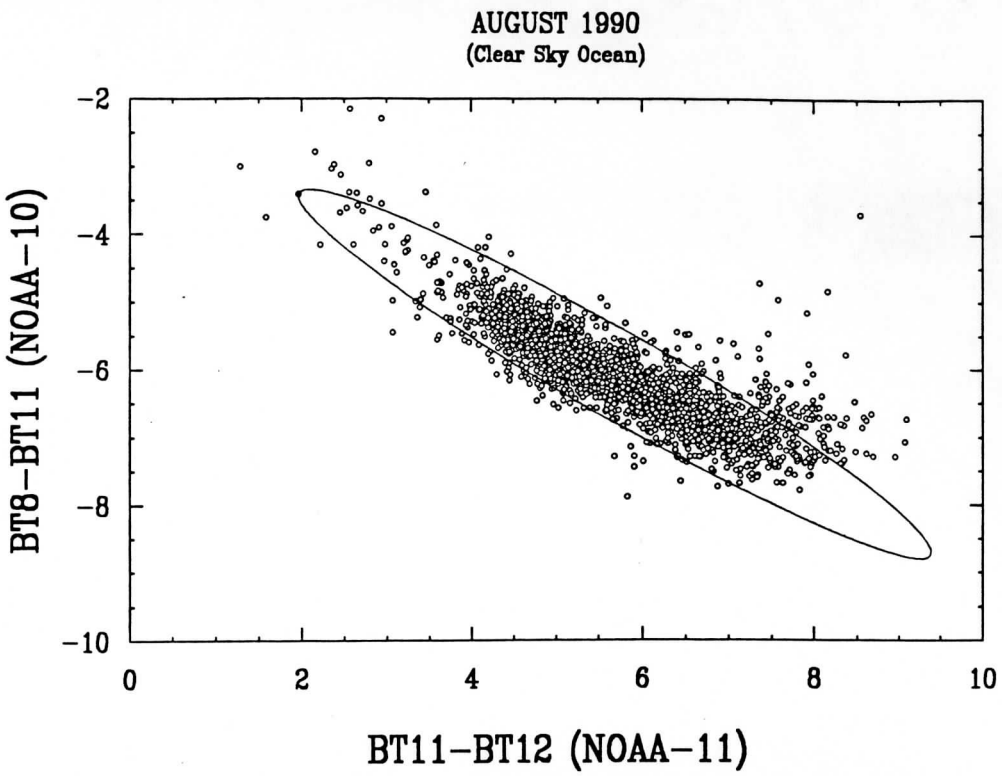

Figure 7. Scatter diagram for the clear-sky August 1990 observations of NOAA-11 brightness temperature difference between 11 and 12 micron versus the NOAA-10 brightness temperature difference between 8.6 and 11 micron. The ellipse represents the 95% confidence limit that points lie within the region.

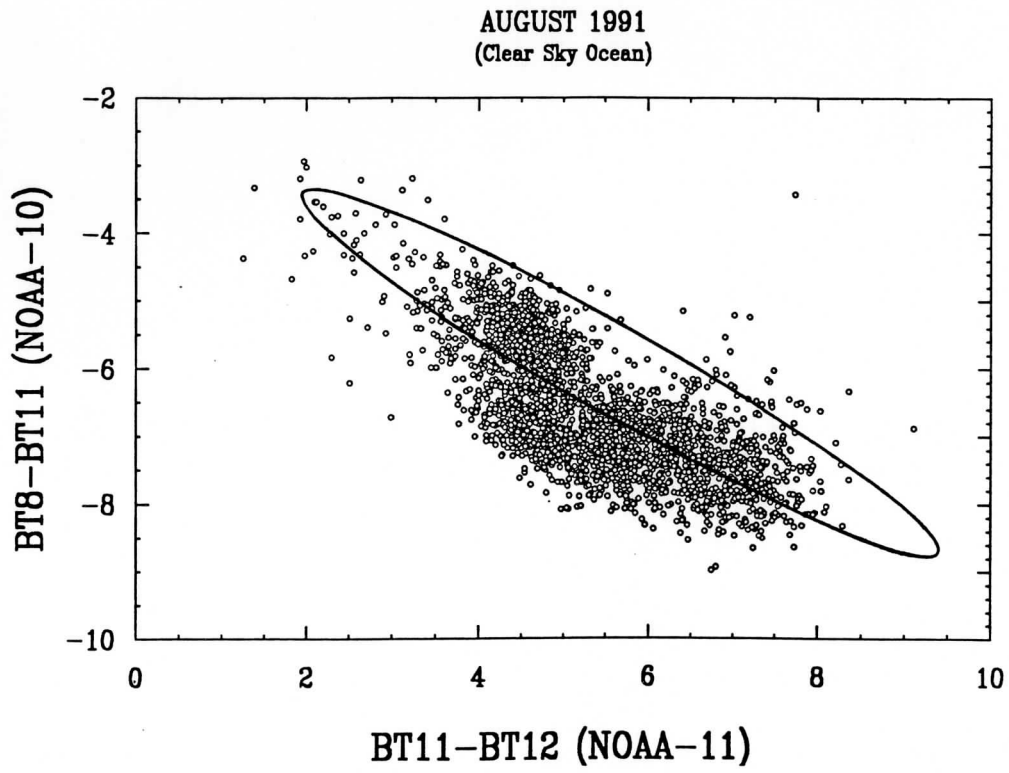

Figure 8. Scatter diagram for cloud-free August 1991 observations of NOAA-11 brightness temperature difference between 11 and 12 micron versus the NOAA-10 brightness temperature difference between 8.6 and 11 micron. The ellipse represents the 95% confidence limit of Figure 7.

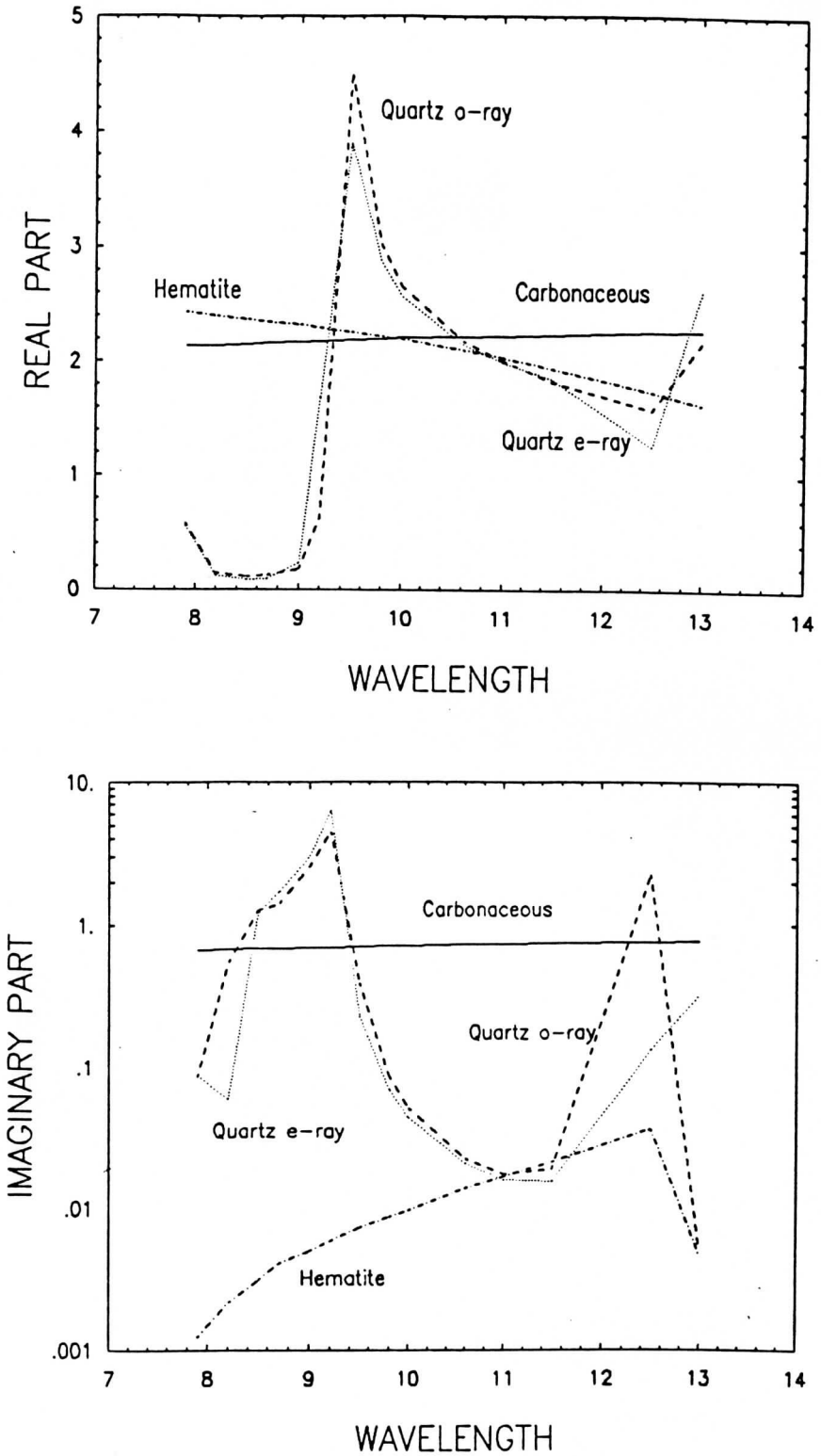

Figure 9. Index of refraction as a function of wavelength (micron) for three elements common in some aerosols.

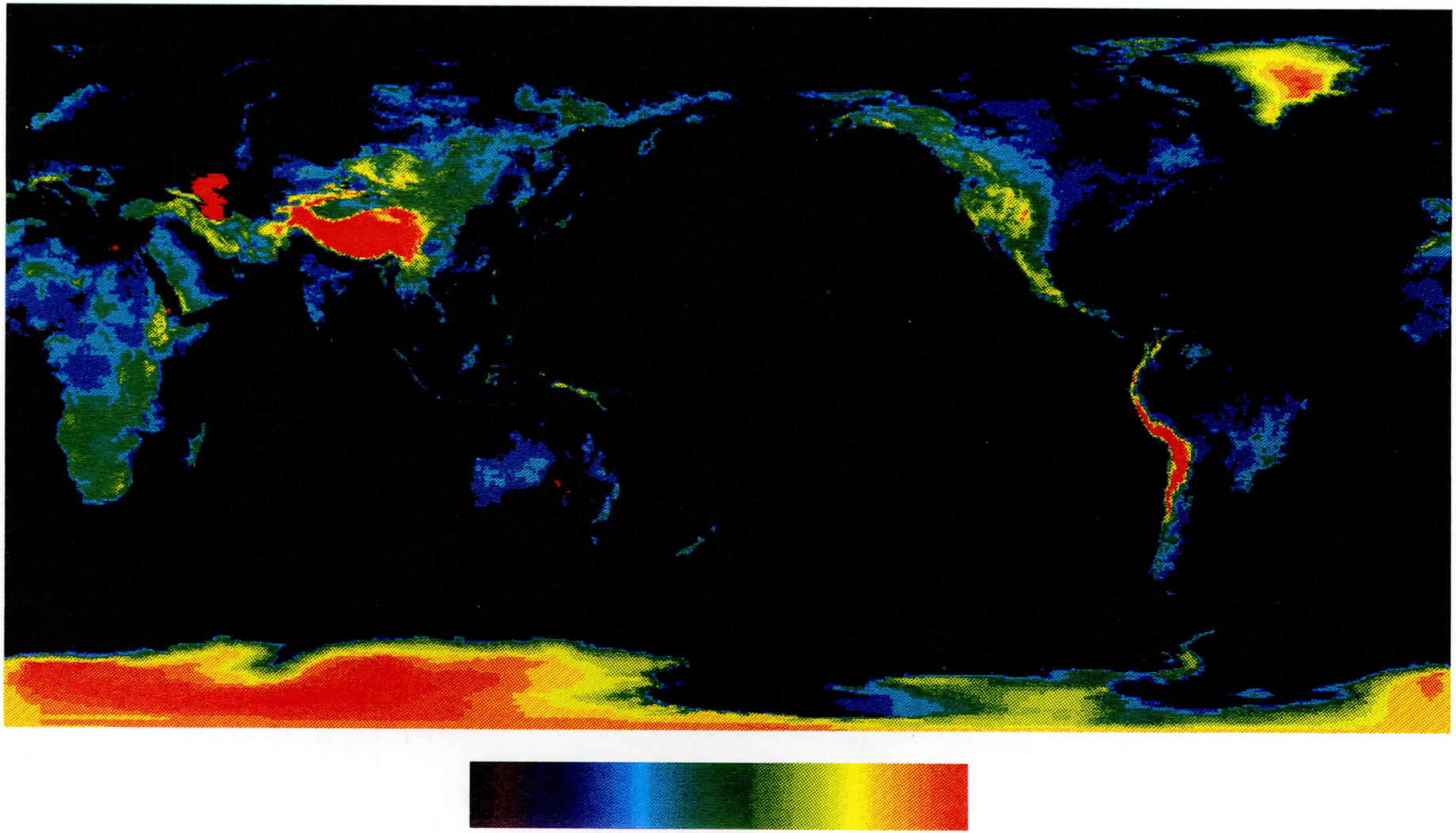

ELEVATION

Figure 10a.

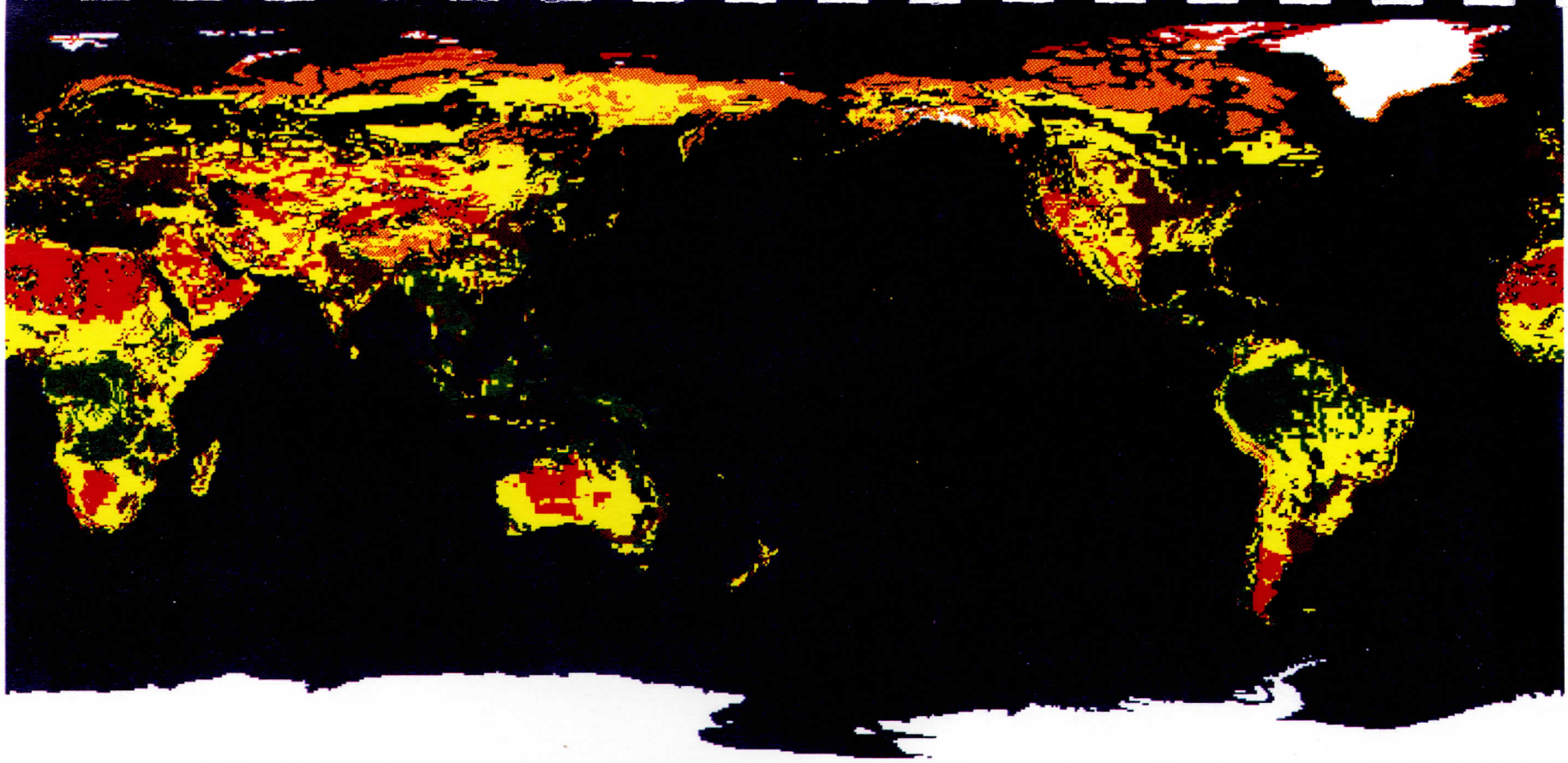

Ecosystem

- Salt Flats
- Ice
- Tundra
- Desert
- Volcanic Islands
- Wetlands
- Conifer Forest
- Deciduous Frorest
- Tropical Rain Forest
- Coastal
- Farm Land
- Grass Land
- City
- Water

Figure 10b.

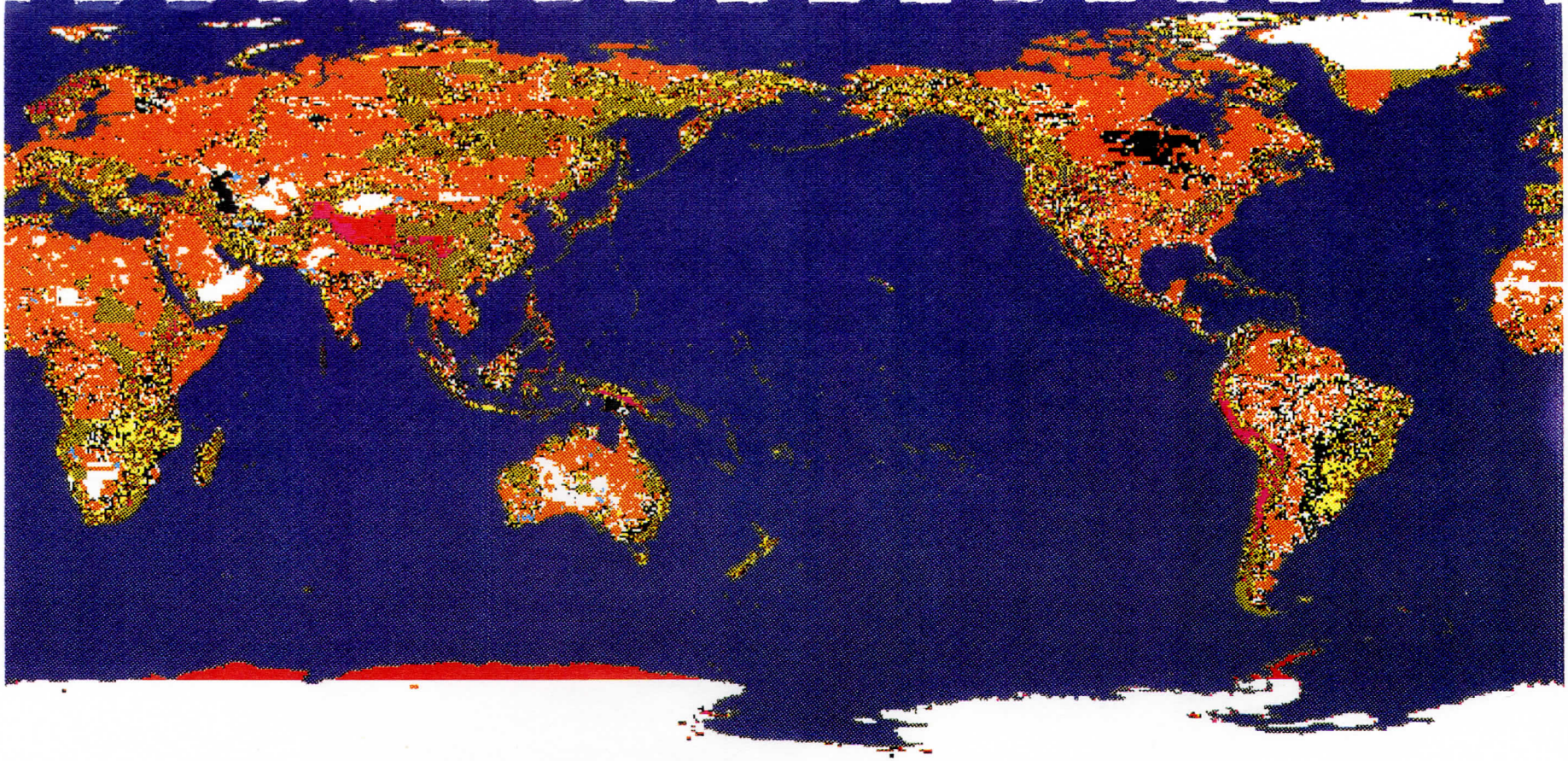
Character
Ocean
No Data
Extrememly Rugged Mountains
Average Mountains
Low Mountains and Hills
Isolated Mountains, Ridge or Peak
Major Valleys or River Beds
Lake Country or Atoll
Marsh
Desert (or for high lats, Glaciers or Permanent Ice)
Flat or Relatively Flat
Salt or Lake Bed

Figure 10c.